

# The Ursa Major Cluster of Galaxies. IV ; HI synthesis observations

Marc A.W. Verheijen<sup>1,2</sup> and Renzo Sancisi<sup>2,3</sup>

<sup>1</sup> NRAO, PO Box O, Socorro, NM 87801, USA

<sup>2</sup> Kapteyn Institute, Postbus 800, 9700 AV, Groningen, The Netherlands

<sup>3</sup> Osservatorio Astronomico di Bologna, Via Ranzani 1, I-40127 Bologna, Italy

Received: 20 November 2000 / Accepted: 4 December 2000

**Abstract.** In this data paper we present the results of an extensive 21cm-line synthesis imaging survey of 43 spiral galaxies in the nearby Ursa Major cluster using the Westerbork Synthesis Radio Telescope. Detailed kinematic information in the form of position-velocity diagrams and rotation curves is presented in an atlas together with HI channel maps, 21cm continuum maps, global HI profiles, radial HI surface density profiles, integrated HI column density maps, and HI velocity fields. The relation between the corrected global HI linewidth and the rotational velocities  $V_{\max}$  and  $V_{\text{flat}}$  as derived from the rotation curves is investigated. Inclination angles obtained from the optical axis ratios are compared to those derived from the inclined HI disks and the HI velocity fields. The galaxies were not selected on the basis of their HI content but solely on the basis of their cluster membership and inclination which should be suitable for a kinematic analysis. The observed galaxies provide a well-defined, volume limited and equidistant sample, useful to investigate in detail the statistical properties of the Tully-Fisher relation and the dark matter halos around them.

**Key words:** Galaxies: fundamental parameters – Galaxies: kinematics and dynamics – Galaxies: spiral – Galaxies: structure

## 1. Introduction

The statistical properties of the Tully-Fisher relation (TFR), like its scatter and slope, and in more detail the characteristics of dark matter halos around galaxies, like their core densities and radii, are of great interest to those who study galaxy formation scenarios. The relevant observables for the TFR are total luminosities and rotational velocities while actual rotation curves and luminosity profiles are required to obtain constraints on the density profiles of dark matter halos. However, the available data sets from which these observables can be obtained are often

suffering from incompleteness, distance uncertainties and inhomogeneous observing and data analysis techniques.

Furthermore, the interpretation of the observables is not always unambiguous. For instance, the rotational velocity of a galaxy is generally inferred from the width of its global HI profile and often this measured width is being related directly to the dark matter potential (e.g Navarro & Steinmetz 2000). However, the width of the HI profile is a complicated convolution of the 2-dimensional distribution of HI in a galaxy disk and the shape and extent of its rotation curve as sampled by the HI gas. Needless to say one has to exercise caution when relating the observed scatter and slope in the TFR to the outcome of numerical and semi-analytical simulations of galaxy formation. This is especially the case when the observed TFR was constructed to serve as an empirical distance estimator and the selection criteria and applied corrections to the raw observables were optimized to linearize the relation and minimize its scatter.

To overcome some of the observational issues, we initiated a program to obtain detailed multi-band photometric and kinematic information on individual galaxies in a well-defined, complete sample. The nearby Ursa Major cluster of galaxies provides a particularly suitable sample. In the first place, the galaxies in the cluster are all at roughly the same distance. Therefore, there is little doubt about their relative luminosities, sizes and masses. Furthermore, the Ursa Major cluster contains overwhelmingly gas-rich systems and the morphological mix of its galaxy members is close to that of the lower density field. A detailed discussion on the definition of the Ursa Major cluster is given by Tully et al. (1996) (Paper I). The characteristics of this cluster will be discussed in more detail in Section 2.

In this paper we present the results of an extensive 21cm-line synthesis imaging survey of individual galaxies in the Ursa Major cluster using the Westerbork Synthesis Radio Telescope (WSRT). The HI data are presented in the form of an atlas. Multi-band optical and near-infrared imaging photometry is presented in Paper I together with B-band and K'-band images of all identified cluster members. Forthcoming papers in this series will use these data

to investigate the TFr while the HI rotation curves will be supplemented in the inner regions with already obtained high resolution optical rotation curves to derive constraints on the structural properties of the dark matter halos and the mass-to-light ratios of the stellar populations.

This data paper is organized as follows. Section 2 describes the Ursa Major cluster in more detail and contains morphological and photometric information on the galaxies observed with the WSRT. Data acquisition and reduction procedures are explained in Section 3. Section 4 explains how the corrected linewidth can be matched to  $V_{\max}$  and  $V_{\text{flat}}$  from the rotation curves through an appropriate correction for turbulent motion. Inclinations are derived from the optical images, HI column density maps and HI velocity fields and Section 5 presents a comparison of these inclinations. The layout of the HI atlas is described in Section 6 with details about the various elements of the atlas pages. The HI properties of the Ursa Major cluster galaxies as a sample are presented in Section 7. Some concluding remarks are given in Section 8.

## 2. The sample

The nearby Ursa Major cluster as defined in Paper I has 79 identified members. It is located in the Supergalactic plane at an angular distance of 38 degrees from the core of the Virgo cluster. It has a recession velocity of  $950 \text{ km s}^{-1}$  and a velocity dispersion of only  $\approx 150 \text{ km s}^{-1}$ . In Paper I and in Tully & Verheijen (1997) (Paper II) a distance of 15.5 Mpc was adopted. However, new HST cepheid distances to local TFr calibrators (e.g. Sakai et al. 2000) and a new correction formalism for internal extinction (Tully et al. 1998) now place the Ursa Major cluster galaxies at a mean distance of 18.6 Mpc (Tully & Pierce 2000). At this distance, 1 arcmin corresponds to 5.4 kpc. The morphological mix of the cluster members is made up overwhelmingly by late type systems and only a dozen lenticulars are known members. Morphological and photometric properties in the optical and near-infrared of individual galaxies are described in detail in Paper I. The galaxy distribution shows no concentration toward any core and no X-ray emitting intra-cluster gas has been detected.

It should be noted that individual galaxies in the nearby Virgo (Warmels 1988a, 1988b; Cayatte et al. 1990), A1367 (Dickey & Gavazzi 1991), Hercules (Dickey 1997) and Coma (Bravo-Alfaro et al. 2000) clusters have also been studied in detail and the effect of the dense environment on the properties of the HI disks in these clusters has been clearly demonstrated. The HI disks in the cores of these rich clusters are in general very small and often offset from the optical galaxy. On the other hand, the volume limited survey of the Hydra cluster (McMahon 1993) does not show such an HI deficiency although some interesting dynamical substructure has been revealed in this system. It should be stressed that the Ursa Major cluster

is markedly different from these more massive and denser clusters. In selecting the Ursa Major sample, these environmental effects are carefully avoided as well as fore- and background contamination caused by high velocity dispersions and complex dynamical and spatial substructures.

Since the Ursa Major galaxies are all at the same distance, the effects of incompleteness and uncertain relative distances are minimized. A complete sample of 62 galaxies brighter than  $M_B \approx -16.8$ , i.e. roughly twice the luminosity of the Small Magellanic Cloud, was constructed and nearly all cluster members were observed with the WSRT. In this paper, however, only those 49 galaxies which are more inclined than 45 degrees, as derived from the optical axis ratio, will be considered for a detailed kinematic study.

Table 1 gives a summary of the positional and morphological properties of these 49 galaxies while photometrics are presented in Table 2, based on a 18.6 Mpc distance. There are 3 additional galaxies in the tables which do not meet the luminosity ( $^f$ ) and inclination ( $^i$ ) criteria but happened to be in the same WSRT fields as galaxies from the complete sample. Of all those 52 galaxies, the HI synthesis data of 30 were fully analyzed. Thirteen systems were observed and detected but the HI data of these galaxies are presented in an abbreviated form comprising only the channel maps, global profiles and position-velocity diagrams. Two of the smaller galaxies were detected in HI but they are confused with the HI emission from their more massive companions. Finally, there are 7 galaxies in the complete sample which have not been observed or detected because of their low HI content known from single dish observations. These are in general S0 or Sa systems.

Table 1 presents the following positional and morphological information:

- Column* (1) gives the NGC or UGC numbers.
- Columns* (2) and (3) provide the equatorial coordinates (B1950) derived from the optical images.
- Columns* (4) and (5) give the Galactic coordinates.
- Column* (6) provides the morphological type.
- Column* (7) gives the observed major axis diameter of the  $25^{\text{th}}$  mag arcsec $^{-2}$  blue isophote.
- Column* (8) contains the position angle of the receding side of the galaxy. For galaxies which are not observed or not detected in HI, this is the smallest position angle of the major axis measured eastward from the north.
- Column* (9) contains the observed ellipticity of the optical galaxy image.
- Column* (10) gives the inclination  $i_{\text{opt}}$  as derived from the observed axis ratio (b/a). See Section 5.1 for further details.
- Column* (11) gives the adopted inclination angle as derived from several methods described in Section 5.
- Column* (12) indicates whether a galaxy has a low (LSB) or high surface brightness (HSB) according to paper II.
- Columns* (13) and (14) provide the galactic extinction in the B-band according to Burstein & Heiles (1984) (BH)

**Table 1.** All galaxies in the Ursa Major cluster brighter than  $M^{b,i}(B)=-16.8$  and more inclined than 45 degrees.

Name	R.A.	Dec.	Galactic		Type	$D_{25}(B)$	PA	$1-b/a$	$i_{opt}$	$i_{adopt}$	S.B.	[BH] mag	$A_B^b$ [SFD] mag
(1)	(2)	(3)	Long.	Lat.	(6)	(7)	(8)	(9)	(10)	(11)	(12)	(13)	(14)
	(1950)					(')	( $^{\circ}$ )		( $^{\circ}$ )	( $^{\circ}$ )		mag	mag
<i>Galaxies with fully analyzed HI data:</i>													
U6399	11 20 35.9	51 10 09	152.08	60.96	Sm	2.40	140	0.72	79	75 $\pm$ 2	LSB	0.00	0.07
U6446	11 23 52.9	54 01 21	147.56	59.14	Sd	2.27	200	0.38	54	51 $\pm$ 3	LSB	0.00	0.07
N3726	11 30 38.7	47 18 20	155.38	64.88	SBc	5.83	194	0.38	54	53 $\pm$ 2	HSB	0.01	0.07
N3769	11 35 02.8	48 10 10	152.72	64.75	SBb	2.97	150	0.69	76	70 $\pm$ 2	HSB	0.01	0.10
U6667	11 39 45.3	51 52 32	146.27	62.29	Scd	3.43	88	0.88	90	89 $\pm$ 1	LSB	0.00	0.07
N3877	11 43 29.3	47 46 21	150.72	65.96	Sc	5.40	36	0.78	84	76 $\pm$ 1	HSB	0.01	0.10
N3893	11 46 00.2	48 59 20	148.15	65.23	Sc	3.93	352	0.33	49	49 $\pm$ 2	HSB	0.02	0.09
N3917	11 48 07.7	52 06 09	143.65	62.79	Scd	4.67	257	0.76	82	79 $\pm$ 2	LSB	0.01	0.09
N3949	11 51 05.5	48 08 14	147.63	66.40	Sbc	2.90	297	0.38	54	55 $\pm$ 2	HSB	0.03	0.09
N3953	11 51 12.4	52 36 18	142.21	62.59	SBbc	6.10	13	0.50	62	62 $\pm$ 1	HSB	0.01	0.13
N3972	11 53 09.0	55 35 56	138.85	60.06	Sbc	3.43	298	0.72	79	77 $\pm$ 1	HSB	0.00	0.06
U6917	11 53 53.1	50 42 27	143.46	64.45	SBd	3.17	123	0.46	59	56 $\pm$ 2	LSB	0.03	0.12
U6923	11 54 14.4	53 26 19	140.51	62.06	Sdm	1.97	354	0.58	68	65 $\pm$ 2	LSB	0.00	0.12
U6930 <sup>i</sup>	11 54 42.3	49 33 41	144.54	65.51	SBd	3.00	39	0.14	32	31 $\pm$ 3	LSB	0.05	0.13
N3992	11 55 00.9	53 39 11	140.09	61.92	SBbc	6.93	248	0.44	58	56 $\pm$ 2	HSB	0.01	0.13
U6940 <sup>f</sup>	11 55 12.4	53 30 46	140.17	62.06	Scd	0.83	135	0.72	79	75 $\pm$ 3	LSB	0.00	0.12
U6962 <sup>i</sup>	11 55 59.5	43 00 44	154.08	71.05	SBcd	2.33	179	0.20	38	37 $\pm$ 3	HSB	0.00	0.09
N4010	11 56 02.0	47 32 16	146.68	67.36	SBd	4.63	65	0.88	90	89 $\pm$ 1	LSB	0.00	0.11
U6969	11 56 12.9	53 42 11	139.70	61.96	Sm	1.50	330	0.69	76	76 $\pm$ 2	LSB	0.01	0.13
U6973	11 56 17.8	43 00 03	153.97	71.10	Sab	2.67	40	0.61	70	71 $\pm$ 3	HSB	0.00	0.09
U6983	11 56 34.9	52 59 08	140.27	62.62	SBcd	3.20	270	0.34	50	49 $\pm$ 1	LSB	0.01	0.12
N4051	12 00 36.4	44 48 36	148.88	70.08	SBbc	5.90	311	0.34	50	49 $\pm$ 3	HSB	0.00	0.06
N4085	12 02 50.4	50 37 54	140.59	65.17	Sc	2.80	255	0.76	82	82 $\pm$ 2	HSB	0.01	0.08
N4088	12 03 02.0	50 49 03	140.33	65.01	Sbc	5.37	231	0.63	71	69 $\pm$ 2	HSB	0.01	0.09
N4100	12 03 36.4	49 51 41	141.11	65.92	Sbc	5.23	344	0.71	77	73 $\pm$ 2	HSB	0.03	0.10
N4102	12 03 51.3	52 59 22	138.08	63.07	SBab	3.00	38	0.44	58	56 $\pm$ 2	HSB	0.01	0.09
N4157	12 08 34.2	50 45 47	138.47	65.41	Sb	6.73	63	0.83	90	82 $\pm$ 3	HSB	0.02	0.09
N4183	12 10 46.5	43 58 33	145.39	71.73	Scd	4.77	346	0.86	90	82 $\pm$ 2	LSB	0.00	0.06
N4217	12 13 21.6	47 22 11	139.90	68.85	Sb	5.67	230	0.74	80	86 $\pm$ 2	HSB	0.00	0.08
N4389	12 23 08.8	45 57 41	136.73	70.74	SBbc	2.50	276	0.34	50	50 $\pm$ 4	HSB	0.00	0.06
<i>Galaxies with partially analyzed HI data:</i>													
N3718	11 29 49.9	53 20 39	147.01	60.22	Sa	7.53	195	0.58	68	69 $\pm$ 3	HSB	0.00	0.06
N3729	11 31 04.9	53 24 08	146.64	60.28	SBab	2.80	164	0.32	48	49 $\pm$ 3	HSB	0.00	0.05
U6773	11 45 22.1	50 05 12	146.89	64.27	Sm	1.53	341	0.47	60	58 $\pm$ 3	LSB	0.00	0.07
N6818	11 48 10.1	46 05 09	151.76	67.78	Sd	2.20	77	0.72	79	75 $\pm$ 3	LSB	0.00	0.09
U6894	11 52 47.3	54 56 08	139.52	60.63	Scd	1.67	269	0.84	90	83 $\pm$ 3	LSB	0.00	0.06
N3985	11 54 06.4	48 36 48	145.94	66.27	Sm	1.40	70	0.37	53	51 $\pm$ 3	HSB	0.05	0.11
N4013	11 55 56.8	44 13 31	151.86	70.09	Sb	4.87	245	0.76	88	90 $\pm$ 1	HSB	0.00	0.07
U7089	12 03 25.4	43 25 18	149.90	71.52	Sdm	3.50	215	0.81	90	80 $\pm$ 3	LSB	0.00	0.07
U7094	12 03 38.5	43 14 05	150.14	71.70	Sdm	1.60	39	0.64	72	70 $\pm$ 3	LSB	0.00	0.06
N4117	12 05 14.2	43 24 17	149.07	71.72	S0	1.53	21	0.56	67	68 $\pm$ 3	LSB	0.00	0.06
N4138	12 06 58.6	43 57 49	147.29	71.40	Sa	2.43	151	0.37	53	53 $\pm$ 3	HSB	0.00	0.06
N4218	12 13 17.4	48 24 36	138.88	67.88	Sm	1.17	316	0.40	55	53 $\pm$ 3	HSB	0.00	0.07
N4220	12 13 42.8	48 09 41	138.94	68.13	Sa	3.63	140	0.69	76	78 $\pm$ 3	HSB	0.00	0.08
<i>Galaxies with confused HI data:</i>													
1135+48	11 35 09.2	48 09 31	152.71	64.77	Sm	1.23	114	0.69	76	73 $\pm$ 3	LSB	0.01	0.10
N3896	11 46 18.6	48 57 10	148.10	65.29	Sm	1.60	308	0.33	49	48 $\pm$ 3	LSB	0.02	0.09
<i>Not observed or too little HI content:</i>													
N3870	11 43 17.5	50 28 40	147.02	63.75	S0a	1.13	17	0.31	47	48 $\pm$ 3	HSB	0.00	0.07
N3990	11 55 00.3	55 44 13	138.25	60.04	S0	1.47	40	0.50	62	63 $\pm$ 3	HSB	0.00	0.07
N4026	11 56 50.7	51 14 24	141.94	64.20	S0	4.37	177	0.74	80	84 $\pm$ 3	HSB	0.04	0.10
N4111	12 04 31.0	43 20 40	149.53	71.69	S0	4.47	150	0.78	84	90 $\pm$ 3	HSB	0.00	0.06
U7129	12 06 23.6	42 01 08	151.00	72.99	Sa	1.27	72	0.31	47	48 $\pm$ 3	HSB	0.00	0.06
N4143	12 07 04.6	42 48 44	149.18	72.40	S0	2.60	143	0.46	59	60 $\pm$ 3	HSB	0.00	0.06
N4346	12 21 01.2	47 16 15	136.57	69.39	S0	3.47	98	0.67	75	77 $\pm$ 3	HSB	0.00	0.06

**Table 2.** Photometrics of all galaxies in the UMa cluster brighter than  $M^{b,i}(\text{B})=-16.8$  and more inclined than 45 degrees.

Name	$m_{\text{B}}^{\text{tot}}$	$m_{\text{R}}^{\text{tot}}$	$m_{\text{I}}^{\text{tot}}$	$m_{\text{K}'}^{\text{tot}}$	$W_{\text{R,I}}^i$	$A_{\text{B}}^i$	$A_{\text{R}}^i$	$A_{\text{I}}^i$	$A_{\text{K}'}^i$	$M_{\text{B}}^{b,i}$	$M_{\text{R}}^{b,i}$	$M_{\text{I}}^{b,i}$	$M_{\text{K}'}^{b,i}$	$D_{25}^{b,i}$
(1)	mag	mag	mag	mag	km/s	mag	mag	mag	mag	mag	mag	mag	mag	(')
<i>Galaxies with fully analyzed HI data:</i>														
U6399	14.33	13.31	12.88	11.09	172	0.47	0.36	0.27	0.06	-17.56	-18.44	-18.77	-20.33	1.84
U6446	13.52	12.81	12.58	11.50	174	0.18	0.14	0.10	0.02	-18.08	-18.72	-18.90	-19.88	2.07
N3726	11.00	9.97	9.51	7.96	331	0.34	0.25	0.20	0.05	-20.76	-21.67	-22.07	-23.45	5.32
N3769	12.80	11.56	10.99	9.10	256	0.67	0.50	0.39	0.09	-19.32	-20.35	-20.80	-22.35	2.34
U6667	14.33	13.11	12.63	10.81	167	0.74	0.58	0.43	0.10	-17.83	-18.87	-19.18	-20.65	2.18
N3877	11.91	10.46	9.72	7.75	335	1.06	0.78	0.62	0.15	-20.60	-21.73	-22.29	-23.76	3.95
N3893	11.20	10.19	9.71	7.84	382	0.31	0.23	0.18	0.04	-20.55	-21.45	-21.86	-23.56	3.67
N3917	12.66	11.42	10.85	9.08	276	0.87	0.64	0.51	0.12	-19.65	-20.63	-21.05	-22.40	3.48
N3949	11.55	10.69	10.28	8.43	321	0.33	0.24	0.20	0.05	-20.22	-20.96	-21.31	-22.98	2.66
N3953	11.03	9.66	9.02	7.03	446	0.60	0.43	0.35	0.08	-21.05	-22.20	-22.74	-24.41	5.38
N3972	13.09	11.90	11.34	9.39	264	0.76	0.56	0.44	0.11	-19.08	-20.05	-20.48	-22.08	2.62
U6917	13.15	12.16	11.74	10.30	224	0.31	0.23	0.18	0.04	-18.63	-19.49	-19.84	-21.10	2.84
U6923	13.91	12.97	12.36	11.04	160	0.28	0.22	0.16	0.04	-17.84	-18.67	-19.20	-20.36	1.67
U6930 <sup>i</sup>	12.70	11.71	11.39	10.33	231	0.08	0.06	0.05	0.01	-18.86	-19.78	-20.07	-21.04	2.98
N3992	10.86	9.55	8.94	7.23	547	0.56	0.40	0.33	0.08	-21.18	-22.28	-22.80	-24.21	6.27
U6940 <sup>f</sup>	16.45	15.65	15.44	13.99	50	0.00	0.00	0.00	0.00	-15.02	-15.77	-15.96	-17.37	0.64
U6962 <sup>i</sup>	12.88	11.88	11.42	10.11	327	0.16	0.11	0.09	0.02	-18.72	-19.64	-20.06	-21.27	2.26
N4010	13.36	12.14	11.55	9.22	254	1.20	0.89	0.70	0.17	-19.30	-20.17	-20.55	-22.31	2.97
U6969	15.12	14.32	14.04	12.58	117	0.20	0.17	0.11	0.02	-16.56	-17.28	-17.48	-18.80	1.19
U6973	12.94	11.26	10.53	8.23	364	0.71	0.52	0.42	0.10	-19.21	-20.67	-21.28	-23.23	2.21
U6983	13.10	12.27	11.91	10.52	221	0.21	0.16	0.12	0.03	-18.58	-19.31	-19.61	-20.87	2.99
N4051	10.98	9.88	9.37	7.86	308	0.28	0.21	0.17	0.04	-20.71	-21.72	-22.18	-23.54	5.45
N4085	13.09	11.87	11.28	9.20	247	0.78	0.58	0.46	0.11	-19.12	-20.11	-20.57	-22.27	2.08
N4088	11.23	10.00	9.37	7.46	362	0.74	0.54	0.43	0.10	-20.95	-21.94	-22.45	-24.00	4.40
N4100	11.91	10.62	10.00	8.02	386	0.97	0.70	0.57	0.14	-20.51	-21.49	-21.97	-23.48	4.07
N4102	12.04	10.54	9.93	7.86	393	0.46	0.34	0.27	0.07	-19.86	-21.20	-21.73	-23.57	2.69
N4157	12.12	10.60	9.88	7.52	399	1.40	1.02	0.82	0.20	-20.72	-21.83	-22.33	-24.04	4.64
N4183	12.96	11.99	11.51	9.76	228	1.01	0.76	0.59	0.14	-19.46	-20.16	-20.46	-21.74	3.13
N4217	12.15	10.62	9.84	7.61	381	1.05	0.76	0.62	0.15	-20.33	-21.54	-22.16	-23.90	4.29
N4389	12.56	11.33	10.87	9.12	212	0.20	0.15	0.12	0.03	-19.05	-20.21	-20.63	-22.27	2.31
<i>Galaxies with partially analyzed HI data:</i>														
N3718	11.28	9.95	9.29	7.47	476	0.77	0.55	0.45	0.11	-20.90	-21.99	-22.54	-24.00	6.30
N3729	12.31	10.94	10.30	8.60	296	0.25	0.18	0.15	0.03	-19.34	-20.62	-21.22	-22.78	2.60
U6773	14.42	13.61	13.15	11.23	112	0.09	0.08	0.05	0.01	-17.09	-17.87	-18.28	-20.14	1.35
U6818	14.43	13.62	13.15	11.70	151	0.39	0.31	0.22	0.05	-17.40	-18.10	-18.46	-19.71	1.69
U6894	15.27	14.31	14.00	12.40	124	0.37	0.31	0.21	0.05	-16.51	-17.39	-17.59	-19.01	1.13
N3985	13.25	12.26	11.81	10.19	180	0.18	0.14	0.10	0.02	-18.39	-19.30	-19.69	-21.19	1.29
N4013	12.44	10.79	9.95	7.68	377	1.10	0.80	0.64	0.15	-20.08	-21.40	-22.07	-23.83	3.61
U7089	13.73	12.77	12.36	11.11	138	0.42	0.34	0.24	0.05	-18.11	-18.96	-19.26	-20.30	2.46
U7094	14.74	13.70	13.22	11.58	76	0.00	0.00	0.00	0.00	-16.67	-17.69	-18.16	-19.78	1.29
N4117	14.05	12.47	11.81	9.98	285	0.00	0.00	0.00	0.00	-17.36	-18.92	-19.57	-21.38	1.29
N4138	12.27	10.72	10.09	8.19	374	0.36	0.26	0.21	0.05	-19.50	-20.93	-21.50	-23.22	2.22
N4218	13.69	12.83	12.41	10.83	150	0.15	0.12	0.09	0.02	-17.88	-18.68	-19.06	-20.55	1.06
N4220	12.34	10.79	10.03	8.36	399	0.94	0.68	0.55	0.13	-20.03	-21.29	-21.91	-23.13	2.85
<i>Galaxies with confused HI data:</i>														
1135+48	14.95	14.05	13.61	11.98	111	0.17	0.15	0.09	0.02	-16.67	-17.51	-17.88	-19.40	0.97
N3896	13.75	12.96	12.47	11.35	83	0.00	0.00	0.00	0.00	-17.69	-18.45	-18.92	-20.01	1.49
<i>Not observed or too little HI content:</i>														
N3870	13.67	12.71	12.16	10.73	127	0.08	0.06	0.04	0.01	-17.83	-18.74	-19.26	-20.64	1.06
N3990	13.53	12.08	11.36	9.54	...	0.00	0.00	0.00	0.00	-17.89	-19.31	-20.02	-21.82	1.28
N4026	11.71	10.25	9.57	7.65	...	0.00	0.00	0.00	0.00	-19.74	-21.16	-21.82	-23.71	3.32
N4111	11.40	9.95	9.25	7.60	...	0.00	0.00	0.00	0.00	-20.01	-21.44	-22.13	-23.76	3.24
U7129	14.13	12.80	12.19	...	...	0.08	0.06	0.04	0.01	-17.36	-18.65	-19.23	...	1.19
N4143	12.06	10.55	9.84	7.86	...	0.00	0.00	0.00	0.00	-19.35	-20.83	-21.54	-23.50	2.30
N4346	12.14	10.69	9.96	8.21	...	0.00	0.00	0.00	0.00	-19.27	-20.70	-21.42	-23.15	2.75

and Schlegel et al. (1998) (SFD) as reported by the NASA Extragalactic Database.

Table 2 presents the following photometric information:

*Column* (1) gives the NGC or UGC numbers.

*Columns* (2)–(5) give the observed total magnitudes in the B, R, I and K' passbands from Paper I.

*Column* (6) contains the corrected HI line widths at the 20% level, used to calculate the internal extinction as explained below.

*Columns* (7)–(10) present the calculated internal extinction corrections in the B, R, I and K' passbands toward face-on  $A_{\lambda}^{i \rightarrow 0}$ , calculated according to Tully et al. (1998):

$$A_{\lambda}^{i \rightarrow 0} = \gamma_{\lambda} \log (a/b)$$

where  $a/b$  is the observed axis ratio of the galaxy as an indication of inclination while  $\gamma_{\lambda}$  depends on the luminosity and is calculated according to

$$\begin{aligned} \gamma_B &= 1.57 + 2.75 (\log W_{R,I}^i - 2.5) \\ \gamma_R &= 1.15 + 1.88 (\log W_{R,I}^i - 2.5) \\ \gamma_I &= 0.92 + 1.63 (\log W_{R,I}^i - 2.5) \\ \gamma_{K'} &= 0.22 + 0.40 (\log W_{R,I}^i - 2.5) \end{aligned}$$

where  $W_{R,I}^i$  is the distance independent HI line width corrected for instrumental resolution as described in Section 3.2, corrected for turbulent motion according to Tully & Fouqué (1985) (TFq hereafter) with  $W_{t,20}=22$  km/s as motivated in Section 4 and corrected for inclination using  $i_{\text{adopt}}$  from Table 1. For dwarf galaxies with  $W_{R,I}^i < 85$  km/s and for lenticulars with no dust features, the value of  $\gamma_{\lambda}$  is set to zero at all passbands.

*Columns* (11)–(14) give the total absolute B, R, I and K' magnitudes corrected for Galactic and internal extinction and a distance modulus of 31.35 corresponding to a distance to the Ursa Major cluster of 18.6 Mpc:

$$M_{\lambda}^{b,i} = m_{\lambda}^{\text{tot}} - A_{\lambda}^b - A_{\lambda}^{i \rightarrow 0} - 31.35$$

where the Galactic extinction  $A_B^b$  is taken from SFD as listed in Table 1. Extinction corrections in the other passbands are made according to the Galactic reddening law given by Cardelli et al. (1989) as summarized by SFD under the Landolt filters in their Table 6. It's given by  $A_R^b/A_B^b = 0.62$ ,  $A_I^b/A_B^b = 0.45$  and  $A_{K'}^b/A_B^b = 0.08$ .

*Column* (15) gives the diameter of the 25<sup>th</sup> mag arcsec<sup>-2</sup> blue isophote corrected for both galactic and internal extinction and projection according to TFq:

$$\text{Log}(D_{25}^{b,i}) = \text{Log}(D_{25}) - 0.22 \text{Log}(D_{25}/d_{25}) + 0.09 A_B^b$$

where  $d_{25}$  is the minor axis diameter at the 25<sup>th</sup> mag arcsec<sup>-2</sup> blue isophote and  $A_B^b$  is taken from SFD.

### 3. Data acquisition and reduction

The HI data presented in this paper were obtained with the Westerbork Synthesis Radio Telescope (WSRT) between 1991 and 1996. The integration times varied between  $1 \times 12^{\text{h}}$  and  $5 \times 12^{\text{h}}$  depending on the required signal-to-noise. The angular resolution at the center of the cluster is  $12'' \times 16''$  or  $1.08 \times 1.44$  kpc at the adopted distance of 18.6 Mpc. The FWHM of the primary beam is 37.4 arcminutes or 202 kpc. As a result, often more than one galaxy was mapped in a single field of view. The observed bandwidth was either 2.5 or 5 MHz, depending on the width of the global profiles. The observations of the NGC3992-group and the NGC4111-group required a broad frequency band of 5 MHz and at the same time also sufficient velocity resolution for the dwarf systems. To comply with the correlator restrictions, those two fields were observed only in one polarization (XX) which allowed for a velocity resolution of 10 km s<sup>-1</sup> but resulted in less sensitivity. During the earlier measurements an on-line Hanning taper was applied but this tapering was abandoned later to obtain the highest possible velocity resolution. The various obtained velocity resolutions (dependent on the correlator restrictions) were 5, 8, 10, 20 or 33 km/s, corresponding to typical rms-noise levels of respectively 3.1, 1.9, 2.9, 1.6 and 1.0 mJy beam<sup>-1</sup> for a single 12<sup>h</sup> observation at the highest angular resolution. The data of NGC4013 were kindly made available by R. Bottema who studied this system in great detail (Bottema 1996 and references therein).

More details on the observational parameters for each field are tabulated in the atlas along with the data. What follows is a brief description of the reduction procedures.

The raw UV-data were calibrated, interactively flagged and Fast Fourier Transformed (FFT) using the NEWSTAR software developed at the NFRA in Dwingeloo. The UV points were weighted according to the local density of points in the UV plane and a Gaussian baseline taper was applied with a FWHM of 2293 (m) which attenuates the longest baseline by 50%. To deal with the frequency dependent antenna pattern, five antenna patterns were calculated for each data cube at a regular frequency separation throughout the bandpass. Pixel sizes of 5 arcsec in RA and  $\frac{5}{\sin(\delta)}$  arcsec in declination ensure an adequate sampling of the synthesized beam,  $12'' \times 12''/\sin(\delta)$ .

After the FFT, the datacubes and antenna patterns were further processed using the Groningen Image Processing SYstem (GIPSY). Several channels at the low and high velocity end of the bandpass were discarded because of their higher noise. As a result, there are 110 or 53 usable channels for a bandpass of 2.5 or 5 MHz respectively, except for the N3992 and N4111 fields which had 110 channels across a 5 MHz bandpass. All datacubes were smoothed to lower angular resolutions of  $30'' \times 30''$  and  $60'' \times 60''$ . This facilitates the detection of extended low

**Table 3.** A comparison of the widths and integrated fluxes from the present WSRT survey and from the literature.

Name (1)	This study					Literature					Ref. (12)
	$W_{20}$ --- km s <sup>-1</sup> --- (2)	$\pm$ (3)	Res. (4)	$\int$ Sdv - Jykm s <sup>-1</sup> - (5)	$\pm$ (6)	$W_{20}$ --- km s <sup>-1</sup> --- (7)	$\pm$ (8)	Res. (9)	$\int$ Sdv - Jykm s <sup>-1</sup> - (10)	$\pm$ (11)	
U6399	188.1	1.4	8.3	10.5	0.3	178	20	22	10.1	1.9	1
U6446	154.1	1.0	5.0	40.6	0.5	162	10	22	45.9	4.1	1
N3718 <sup>(c)</sup>	492.8	1.0	33.2	140.9	0.9	480	10	5.5	84.9	26.4	1
						508 <sup>m</sup>	..	33	120	...	8 <sup>WSRT</sup>
N3726	286.5	1.6	5.0	89.8	0.8	290	10	5.5	83.9	10.8	1
N3729 <sup>noSD</sup>	270.8	1.5	33.2	5.5	0.3	...	..	..	...	...	..
						279 <sup>m</sup>	..	33	25 <sup>?</sup>	...	8 <sup>WSRT</sup>
N3769 <sup>i</sup>	265.3	6.7	8.3	62.3	0.6	276	20	7.4	44.1	4.2	2
U6667	187.5	1.4	5.0	11.0	0.4	210	20	22	11.6	2.2	1
N3877	373.4	5.0	33.2	19.5	0.6	352	10	22	24.8	5.6	1
U6773	110.4	2.3	8.3	5.6	0.4	118	8	22	5.6	0.7	6
N3893 <sup>(c)</sup>	310.9	1.0	5.0	69.9	0.5	313	8	22	85.3	5.1	1
N3917	294.5	1.9	8.3	24.9	0.6	284	10	22	21.9	4.7	1
U6818	166.9	2.3	8.3	13.9	0.2	168	15	22	14.8	2.1	1
N3949	286.5	1.4	8.3	44.8	0.4	289	10	22	42.7	5.4	1
N3953 <sup>l</sup>	441.9	2.4	33.1	39.3	0.8	423	10	22	41.0	3.9	1
U6894	141.8	1.1	8.3	5.8	0.2	159	20	7.4	5.1	1.7	2
N3972	281.2	1.4	8.3	16.6	0.4	270	15	22	14.0	2.6	1
U6917	208.9	3.2	8.3	26.2	0.3	211	10	22	31.5	4.1	1
N3985	160.2	3.7	8.3	15.7	0.6	168	..	22	14.1	0.9	5
U6923	166.8	2.4	10.0	10.7	0.6	175	15	22	8.2	2.9	1
						189 <sup>m</sup>	15	41.4	15.6	...	12 <sup>VLA</sup>
U6930	136.5	0.5	8.3	42.7	0.3	145	8	22	38.2	3.5	1
N3992 <sup>l</sup>	478.5	1.4	10.0	74.6	1.5	480	10	22	81.2	5.3	1
						507 <sup>m</sup>	15	41.4	79.9	...	12 <sup>VLA</sup>
U6940	59.3	3.8	10.0	2.1	0.3	226	..	22	7.0	1.0	3
						121 <sup>m</sup>	15	41.4	2.7	...	12 <sup>VLA</sup>
N4013	425.0	0.9	33.0	41.5	0.2	403	10	22	33.8	3.7	1
U6962 <sup>(c)</sup>	220.3	6.6	8.3	10.0	0.3	...	..	22	21.6	4.4	1
						235	..	33	9.2	1.0	4 <sup>WSRT</sup>
N4010	277.7	1.0	8.3	38.2	0.3	281	10	22	38.1	3.4	1
U6969 <sup>c</sup>	132.1	6.4	10.0	6.1	0.5	146	..	13.2	6.0	1.4	3
						159 <sup>m</sup>	15	41.4	6.9	...	12 <sup>VLA</sup>
U6973 <sup>noSD</sup>	367.8	1.8	8.3	22.9	0.2	...	..	..	...	...	..
						408	..	33	18.3	1.2	4 <sup>WSRT</sup>
U6983	188.4	1.3	5.0	38.5	0.6	205	10	22	36.2	4.4	1
N4051 <sup>l</sup>	255.4	1.8	5.0	35.6	0.8	274	15	22	43.4	3.3	1
N4085 <sup>c</sup>	277.4	6.6	19.8	14.6	0.9	299	20	7.4	23.3	2.5	2
						311 <sup>m</sup>	..	33	24 <sup>l</sup>	...	13 <sup>WSRT</sup>
N4088 <sup>(c)</sup>	371.4	1.7	19.8	102.9	1.1	381	8	22	109.2	6.4	1
						378 <sup>m</sup>	..	33	128 <sup>l</sup>	...	13 <sup>WSRT</sup>
U7089 <sup>(c)</sup>	156.7	1.7	10.0	17.0	0.6	162	10	22	17.8	2.2	1
						176	..	33.4	18.9	...	11 <sup>WSRT</sup>
N4100	401.8	2.0	19.9	41.6	0.7	420	20	22	54.0	7.3	1
U7094 <sup>c</sup>	83.7	1.7	10.0	2.9	0.2	112	8	22	6.0	0.6	6
						153 <sup>?</sup>	..	33.4	2.5	...	11 <sup>WSRT</sup>
N4102	349.8	2.0	8.3	8.0	0.2	327	20	7.4	10.3	2.1	2
N4117 <sup>noSD</sup>	289.4	7.5	10.0	6.9	1.1	...	..	..	...	...	..
						314	..	33.4	5.3	...	11 <sup>WSRT</sup>
N4138	331.6	4.5	19.9	19.2	0.7	354 <sup>m</sup>	30	6.8	16	...	14
						340	5	5.2	20.6	0.3	7 <sup>VLA</sup>
N4157 <sup>(c),l</sup>	427.6	2.2	19.9	107.4	1.6	436	10	22	123.9	9.5	1
N4183	249.6	1.2	8.3	48.9	0.7	258	10	22	49.6	5.3	1
N4218	138.0	5.0	8.3	7.8	0.2	160	20	13	5.7	0.9	9
N4217	428.1	5.1	33.2	33.8	0.7	426	20	22	51.8	7.2	1
N4220	438.1	1.3	33.1	4.4	0.3	382 <sup>m</sup>	..	11	3.3	...	10
N4389	184.0	1.5	8.3	7.6	0.2	174	20	7.4	7.6	0.8	2

**Table 3.** (cont.) Notes

---

$(c)$	the authors suggest possible confusion with a dwarf companion.	
$c$	flagged by the authors as confused with near companion.	
$l$	large correction factor ( $>1.20$ ) applied for primary beam flux attenuation.	
$i$	flagged by the authors as possibly interacting.	
$noSD$	no useful single dish profile available due to obvious confusion.	
$m$	line width directly measured from the published HI profile.	
$!$	the integrated flux as quoted by the author is a factor 2 larger than is quoted by any other source. Therefore, half the integrated flux was adopted from this source.	
$WSRT$	synthesis observation with the WSRT.	
$VLA$	synthesis observation with the VLA.	
References :	1: Fisher & Tully (1981)	8: Schwarz (1985)
	2: Appleton & Davies (1982)	9: Thuan & Martin (1981)
	3: Richter & Huchtmeier (1991)	10: Magri (1994)
	4: Oosterloo & Shostak (1993)	11: Van der Burg (1987)
	5: Huchtmeier & Richter (1986)	12: Gottesman et al. (1984)
	6: Schneider et al. (1992)	13: Van Moorsel (1983)
	7: Jore et al. (1996)	14: Grewing & Mebold (1975)

---

level HI emission and the identification of the ‘continuum’ channels which are free from line emission.

### 3.1. The radio continuum emission

The channels free from HI emission were averaged and the resulting continuum map was subtracted from all channels in the data cube. The residuals of the frequency dependent grating rings were only a minor fraction of the noise in the channels containing the line emission. The dirty continuum maps were cleaned (Högbom 1974) down to  $0.3\sigma$ . The clean-components were restored with a gaussian beam of similar FWHM as the synthesized beam. When radio continuum emission from a galaxy was detected, its continuum flux was determined from the cleaned continuum map. In cases of no detection, an upper limit for extended emission was derived by calculating the rms scatter in the flux values obtained by integrating the noise in each of fifteen elliptical areas enclosed by the 25<sup>th</sup> mag blue isophote and positioned at various emission-free regions in the map.

### 3.2. The HI channel maps and the global HI profiles

At all three spatial resolutions, the regions of HI emission were defined by the areas enclosed by the  $2\sigma$  contours in the ‘dirty’ 60” resolution maps. Grating rings and noise peaks above this level were removed manually. The selected regions were enlarged by moving their boundaries 1 arcmin outwards to account for possible emission in the sidelobes. The resulting masks vary from channel to channel in shape, size and position due to the rotation of the HI disk. These masks defined the regions that were cleaned down to  $0.3\sigma$  at all three spatial resolutions.

The clean-components were restored with a Gaussian beam of similar FWHM as the synthesized beam. The

global HI profiles were derived by determining the primary beam corrected flux in each cleaned region. Since the size and shape of the clean masks vary as a function of velocity, the uncertainty in the flux densities at each velocity in the global HI profile varies as well. The noise on the global HI profile was determined by projecting each clean mask at nine different line-free positions in a channel map and integrating over each of them.

For further analysis, each profile was divided up in three equal velocity bins in which the peak fluxes  $F_{low}^{peak}$ ,  $F_{mid}^{peak}$  and  $F_{high}^{peak}$  were determined for the low, middle and high velocity bin respectively. These three peak fluxes were then used to classify a global profile shape according to:

$$\begin{aligned}
 \text{Double peaked} & : F_{low}^{peak} > F_{mid}^{peak} < F_{high}^{peak} \\
 \text{Gaussian} & : F_{low}^{peak} < F_{mid}^{peak} > F_{high}^{peak} \\
 \text{Distorted} & : F_{low}^{peak} < F_{mid}^{peak} < F_{high}^{peak} \\
 & \text{or } F_{low}^{peak} > F_{mid}^{peak} > F_{high}^{peak} \\
 \text{Boxy} & : F_{low}^{peak} \approx F_{mid}^{peak} \approx F_{high}^{peak}
 \end{aligned}$$

In case of a double peaked profile, the peak fluxes on both sides were considered separately when calculating the 20% and 50% levels. In all other cases, the overall peak flux was used. The four velocities  $V_{low}^{20\%}$ ,  $V_{low}^{50\%}$ ,  $V_{high}^{50\%}$  and  $V_{high}^{20\%}$  corresponding to these 20% and 50% levels were determined by linear interpolation between the data points, going from the center outward. In the few cases of non-monotonically decreasing edges, this procedure tends to slightly underestimate the widths. The widths are calculated according to

$$W_{20} = V_{high}^{20\%} - V_{low}^{20\%} \text{ and } W_{50} = V_{high}^{50\%} - V_{low}^{50\%}.$$

The systemic velocity is calculated according to

$$V_{\text{sys}} = 0.25 \left( V_{\text{low}}^{20\%} + V_{\text{low}}^{50\%} + V_{\text{high}}^{50\%} + V_{\text{high}}^{20\%} \right)$$

Because in interferometric measurements some flux may be lost due to the missing short baselines, it is useful to compare the widths and flux densities from the WSRT profiles with those from published single dish observations. However, a meaningful comparison requires that the profile widths are all corrected in the same way for instrumental broadening. In general, the widths that are published by various authors were corrected for instrumental broadening using nearly as many different methods. Therefore, the published line widths had to be de-corrected first to ensure a uniformly applied correction. The de-corrected widths and integrated HI fluxes from the literature are compiled in columns (7)–(11) of Table 3 along with the results from this study in columns (2)–(6).

*Column* (1) gives the NGC or UGC numbers.

*Columns* (2,3) and (7,8) give the widths of the global profiles at the 20% levels and the formal uncertainties.

*Columns* (4) and (9) give the velocity resolutions of the observations.

*Columns* (5,6) and (10,11) contain the integrated HI fluxes derived from the global profiles.

*Column* (12) provides the references to the literature sources.

In case the authors suggest that the single dish profile of a particular galaxy may be confused and synthesis data on that galaxy do exist, these synthesis data are included as well and used in the following comparison. However, first it will be explained how the observed linewidths are corrected for the different instrumental resolutions.

### 3.2.1. Correcting $W_{20}$ for instrumental broadening

The most widely used method to correct for broadening of the global HI profiles due to a finite instrumental velocity resolution was provided by Bottinelli et al. (1990). For the widths at the 20% and 50% levels of the peak flux they advocate the following linear relations:

$$\begin{aligned} W_{20,R} &= W_{20} - \delta W_{20} = W_{20} - 0.55 R \\ W_{50,R} &= W_{50} - \delta W_{50} = W_{50} - 0.13 R \end{aligned}$$

where  $W_{20}$  is the observed linewidth and  $W_{20,R}$  is the linewidth corrected for the instrumental velocity resolution  $R$  in km/s. This empirical prescription is based on comparing linewidths obtained at different resolutions.

However, the correction method applied here deviates from Bottinelli et al.'s method and is based on more analytic considerations. It is easy to imagine that both edges of an intrinsic global profile, when chopped off at their peaks and glued together, approximate a Gaussian with dispersion  $\sigma_0$ . The width at the 20% level of this 'true' Gaussian is then given by

$$W_{20,R} = \sigma_0 \sqrt{8 \ln(5)}$$

A spectral Hanning smoothing was applied to most of the WSRT observations presented in this paper. This smoothing function can also be approximated by a Gaussian with a FWHM equal to the instrumental velocity resolution  $R$  and has a dispersion  $\sigma_R$

$$\sigma_R = \frac{R}{\sqrt{8 \ln(2)}}$$

The dispersion  $\sigma_c$  of the convolved observed Gaussian is then given by

$$\sigma_c = \sqrt{\sigma_0^2 + \sigma_R^2}$$

and the 20% line width of this convolved or observed Gaussian is given by

$$\begin{aligned} W_{20} &= \sigma_c \sqrt{8 \ln(5)} \\ &= \sqrt{8 \ln(5)} \cdot \sqrt{\sigma_0^2 + \sigma_R^2} \\ &= \sqrt{8 \ln(5)} \cdot \sqrt{\sigma_0^2 + \frac{R^2}{8 \ln(2)}} \end{aligned}$$

So, at the 20% level, the intrinsic width  $W_{20,R}$  is broadened to  $W_{20}$  by  $\delta W$  given by

$$\begin{aligned} \delta W_{20} &= W_{20} - W_{20,R} \\ &= \sqrt{8 \ln(5)} \cdot \sqrt{\sigma_0^2 + \frac{R^2}{8 \ln(2)}} - \sigma_0 \sqrt{8 \ln(5)} \\ &= \sigma_0 \sqrt{8 \ln(5)} \cdot \left[ \sqrt{1 + \frac{(R/\sigma_0)^2}{8 \ln(2)}} - 1 \right] \end{aligned}$$

The broadening  $\delta W_{20}$  does not only depend on the instrumental resolution  $R$  but also on the steepness of the slopes of the edges of the profile, expressed by  $\sigma_0$ . Fitting Gaussians to the edges of a profile yields  $\sigma_c$  from which  $\sigma_0$  can be calculated given the known value of  $\sigma_R$ . The equation above can be rewritten using  $\sigma_c$  instead which results in

$$\delta W_{20} = \sigma_c \sqrt{8 \ln(2)} \left( \frac{\ln(5)}{\ln(2)} \right)^2 \left[ 1 - \sqrt{1 - \frac{(R/\sigma_c)^2}{8 \ln(2)}} \right]$$

However, no Gaussians were fitted to the edges of the new WSRT profiles. Instead it is assumed that the slopes of the edges of the profiles are more or less determined by the turbulent motion of the gas with a canonical velocity dispersion of  $\sigma_0 = 10 \text{ km s}^{-1}$ . This results in

$$\delta W_{20} = 35.8 \cdot \left[ \sqrt{1 + \left( \frac{R}{23.5} \right)^2} - 1 \right]$$

and similarly for the 50% level



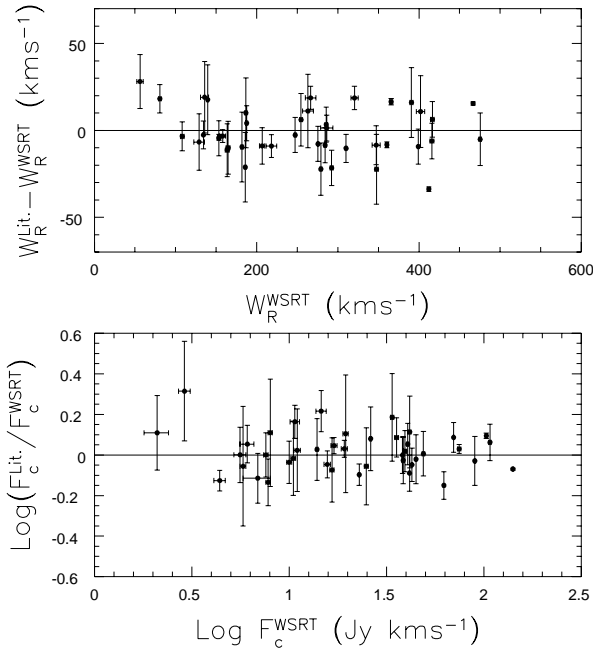


**Fig. 1.** A comparison of the present WSRT results with pre-existing single dish and synthesis data from the literature.

$$\delta W_{50} = 23.5 \cdot \left[ \sqrt{1 + \left( \frac{R}{23.5} \right)^2} - 1 \right]$$

The differences between Bottinelli et al.’s linear prescription and our corrections ( $\Delta\delta W = \delta W^{Bot} - \delta W^{our}$ ) are only minor and tabulated below for typical instrumental resolutions of the WSRT.

level	$\Delta\delta W$				
	----- R (km/s) -----				
	5.0	8.3	16.5	19.9	33.1
20%	2.0	2.4	1.2	0.2	-7.8
50%	0.2	-0.3	-3.1	-4.7	-12.8

The larger differences occur for the poorest resolutions at which only the broadest profiles were observed. Consequently, the differences are a negligible fraction of the line widths.

Figure 1 shows the comparison of the widths and integrated fluxes derived from the new WSRT global profiles and those from the literature. There are no significant systematic differences. The unweighted average difference in widths is  $-0.9 \pm 2.1 \text{ km s}^{-1}$  with a rms scatter of  $14 \text{ km s}^{-1}$ . The unweighted average difference in integrated flux is  $4.7 \pm 3.5$  percent with a rms scatter of 25 percent. It can therefore be concluded that on average the WSRT results are in excellent agreement with the results from single dish observations.

### 3.3. The total HI maps

As a next step, the total integrated HI maps were constructed from the *cleaned* datacubes. The *clean*-masks were used to define the regions with HI emission. Outside these regions, the pixels were set to zero and all the channels containing a non-zero area were added to build up the integrated column density map. This was then corrected for attenuation by the primary beam. Although the advantage of this procedure is a higher signal-to-noise ratio at a certain pixel in the HI map, the disadvantage is that the noise is no longer uniform across the map. As a result, the  $3\sigma$ -contour level in an integrated HI map is not defined. Signal-to-noise maps have been made, however, using the prescription outlined in Appendix A and the average pixel value of all pixels with  $2.75 < (\frac{S}{N}) < 3.25$  was determined. This average value was adopted as the ‘ $3\sigma$ ’ level for the column density.

### 3.4. The radial HI surface density profiles

The integrated column density maps were used to derive the radial HI surface density profiles by azimuthally averaging in concentric ellipses. The orientations and widths of the ellipses were the same as those of the projected tilted rings fitted to the HI velocity field (see Section 3.6.1). In the case of a warp with overlapping ellipses, the flux in the overlapping regions was proportionally assigned to each ellipse. The azimuthal averaging was done separately for the receding and approaching halves of each tilted ring to reveal possible asymmetries. Pixels in the HI map without any measured signal were set to zero. Finally, the entire radial profile was scaled by the total HI mass as derived from the global HI profile. No attempt was made to correct the profiles for the effect of beam smearing.

This method for extracting the surface density profiles from integrated HI maps breaks down for nearly edge-on systems; the highly inclined annuli with large major axis diameters could still pick up some flux along the minor axis due to beam smearing. In such cases, Lucy’s (1974) iterative deprojection scheme as adapted and developed by Warmels (1988b) might be preferable.

Due to the complex noise structure of the integrated HI map, no attempt was made to estimate the errors on the radial HI surface density profiles.

### 3.5. The HI velocity fields

The HI data cubes were smoothed to velocity resolution of  $\approx 19 \text{ km s}^{-1}$  in order to obtain a good spectral signal-to-noise ratio. HI velocity fields were then constructed by fitting single Gaussians to the velocity profiles at each pixel. Initial estimates for the fits were given by the various moments of the profiles determined over the velocity range covered by the masks. Only those fits were accepted for which 1) the central velocity of the fitted Gaussian lies

inside the masked volume, 2) the amplitude is larger than five times the rms noise in the profile and 3) the uncertainty in the central velocity is smaller than  $\frac{1}{3}$  the velocity resolution.

Due to projection effects and beam smearing, the velocity profiles in highly inclined systems and in the central regions of galaxies may deviate strongly from a Gaussian shape. The exact shape depends on the spatial and kinematic distribution of the gas within a synthesized beam. Fitting single Gaussians to these usually skewed profiles results in an underestimate of the rotational velocity at that position. As a consequence, the gradients in the velocity field become shallower. There are several methods to correct for the effects of beam smearing. In the present cases, however, the signal-to-noise was in general too low to allow a useful application of these methods, and, since only a small number of systems were recognized as seriously affected, the HI velocity fields were not corrected for the effects of beam smearing.

### 3.6. Rotation curves

The rotation curves were derived in two ways; 1) by fitting tilted-rings to the velocity fields (Begeman 1987) and 2) by estimating the rotational velocities by eye from the position-velocity diagrams.

#### 3.6.1. using the velocity fields

The determination of the rotation curves from the velocity fields was done in three steps by fitting tilted rings to the velocity field (see Begeman 1987, 1989). The widths of the rings were set at  $\frac{2}{3}$  of the width of the synthesized beam (i.e. 10", 20" or 40").

First, the systemic velocity and the dynamical center were determined. In this first step the inclination and position angles were the same for each ring and kept fixed at the values derived from the optical images. The systemic velocity, center and rotational velocity were fitted for each ring. All the points along the tilted ring were considered and weighted uniformly. In general, no significant trend as a function of radius could be detected for the systemic velocity and center. The adopted values were calculated as the average of all rings.

Second, the systemic velocity and center of rotation were kept fixed for each ring while the position angle, inclination and rotational velocity were fitted. All the points along the tilted ring were considered but weighted with  $\cos(\theta)$  where  $\theta$  is the angle in the plane of the galaxy measured from the receding side. Hence, points along the minor axis have zero weight. While the position angle can be determined accurately, the inclination and rotational velocity are rather strongly correlated for inclinations below 60 degrees and above 80 degrees (Begeman 1989). As a result, the fitted inclinations can vary by a large amount from one ring to another. However, a possible trend in the

inclination with radius due to a central bar or a warp can be detected. A change in inclination angle often goes together with a change in the more accurately determined position angle.

Third, the rotational velocity was fitted again for each ring while keeping the systemic velocity, center of rotation, inclination and position angle fixed. Again, all the points along the tilted ring were considered but weighted with  $\cos(\theta)$ . The fixed values for the inclination and position angles were determined in the second step by averaging the solutions over all the rings or fixing a clear trend. For nearly edge-on galaxies, the inclinations determined in the second step were often overruled by higher values based on the clear presence of a dust lane (e.g. N4010, N4157, N4217) or the very thin distribution of gas in the column density maps (e.g. U6667). However, uncertainty in the inclinations of nearly edge-on systems does not significantly influence the amplitude of the rotational velocity.

The results of this 3-step procedure were used to construct a model velocity field. This model was subtracted from the actual observed velocity field to yield a map of the residual velocities. In some cases (e.g. N3769, N4051, N4088) this residual map shows significant systematic residuals, indicative of non-circular motion or a bad model fit due to a noisy observed velocity field. As a further check, the derived rotation curve is projected onto the position-velocity maps along the major and minor axis.

The errors on the inclination and position angles and the rotational velocity are formal errors. They do not include possible systematic uncertainties due to, for instance, the beam smearing.

#### 3.6.2. using the position-velocity diagrams

It has already been remarked (see Section 3.5) that beam smearing affects the determination of the velocity fields, especially in the central regions of galaxies and in highly inclined disks. As a consequence, the rotation curves derived from such velocity fields are underestimated as one can see from their projection on the XV-maps. In order to overcome this problem, the rotation curves were derived directly from the major axis XV-maps in a manner similar to that used for edge-on systems (cf. Sancisi & Allen 1979). This was done by two independent human neural networks trained to estimate the maximum rotational velocity from the asymmetric velocity profiles, taking into account the instrumental band- and beam-widths and the random gas motions. This was done for both the receding and approaching side of a galaxy. The rotation curves were then deprojected (also accounting for possible warps) by using the same position and inclination angles as fixed in the third step described in the previous section. In general, the average rotation curves derived from the XV-diagrams are in reasonable agreement with those obtained by the tilted ring fits. As expected, significant differences

can only be noted for galaxies which are highly inclined or have a steeply rising rotation curve.

From the XV-diagrams it is clear that many galaxies have kinematic asymmetries in the sense that the rotation curve often rises more steeply on one side of a galaxy than on the other side (e.g. N3877, N3949). The rotation curves as derived from the velocity fields and XV-diagrams are tabulated in Table 4 for the approaching and receding parts separately. The adopted changes in inclination and position angles of N3718 and N4138 are motivated in the notes on the atlas pages of these galaxies. The uncertainties quoted in Table 4 are not 1-sigma Gaussian errors but rather reflect fiducial velocity ranges, based on the position-velocity diagrams.

#### 4. Matching HI linewidths to $V_{\max}$ and $V_{\text{flat}}$

In this section, it will be investigated how the linewidth correction for turbulent motion can be used to match the finally corrected global HI linewidths to the actual rotational velocities measured from the rotation curves.

After the correction for instrumental resolution, the profile widths are generally corrected for broadening due to turbulent motions of the HI gas by applying TFq's formula

$$W_{R,l}^2 = W_l^2 + W_{t,l}^2 \left[ 1 - 2 e^{-\left(\frac{W_l}{W_{c,l}}\right)^2} \right] - 2 W_l W_{t,l} \left[ 1 - e^{-\left(\frac{W_l}{W_{c,l}}\right)^2} \right]$$

where the subscript  $l$  refers to the widths at the  $l=20\%$  or the  $l=50\%$  level of peak flux. This formula yields a linear subtraction of  $W_{t,l}$  if  $W_l > W_{c,l}$  and a quadratic subtraction if  $W_l < W_{c,l}$ . Values of  $W_{t,l}$  and  $W_{c,l}$  are different for line width corrections at the 20% and 50% levels. The values of  $W_{c,l}$  indicate the profile widths where the transition from a boxy to a Gaussian shape occurs. The amount by which a global profile is broadened due to random motions is given by  $W_{t,l}=2k_l\sigma$  where, for a Gaussian velocity dispersion  $\sigma$ ,  $k_{20}=1.80$  and  $k_{50}=1.18$ .

The generally adopted values for  $W_{c,l}$  are  $W_{c,20}=120$  km/s and  $W_{c,50}=100$  km/s. The more important values of  $W_{t,l}$ , however, have been subject of some debate among various authors. With our new HI synthesis data we can give a meaningful contribution to this debate.

Bottinelli et al. (1983) came up with an empirical approach, based on a minimization of the scatter in the TF-relation. They assumed an anisotropic velocity dispersion of the HI gas of  $\sigma_x=\sigma_y=1.5\sigma_z$  and a velocity dispersion perpendicular to the plane of  $\sigma_z=10$  km/s. They determined the values of  $k_l$  by minimizing the scatter in the TF-relation and found  $k_{20}=1.89$  and  $k_{50}=0.71$ , indicating deviations from a Gaussian distribution (broader wings).

**Table 4.** Rotation curves derived from velocity fields and XV-diagrams.

Rad. (")	$V_{\text{rot}}^{\text{app}}$ km/s	+/-	$V_{\text{rot}}^{\text{rec}}$ km/s	+/-	$V_{\text{rot}}^{\text{ave}}$ km/s	i (°)	PA (°)		
<u>U6399</u>									
10	25	12	7	25	10	7	25	75	141
20	44	10	7	49	7	7	46	75	141
30	61	12	7	61	7	5	61	75	141
40	70	7	5	69	5	5	70	75	141
50	77	7	5	78	3	5	78	75	141
60	82	10	5	84	5	5	83	75	141
70	84	5	5	-	-	-	84	75	141
80	86	5	5	-	-	-	86	75	141
90	88	5	5	-	-	-	88	75	141
<u>U6446</u>									
10	39	8	8	23	10	10	31	51	188
20	49	8	8	61	8	10	55	51	188
30	57	5	5	65	5	8	61	51	188
40	63	5	5	65	5	8	64	51	188
50	69	8	5	65	5	5	67	51	188
60	71	5	5	70	5	5	70	51	188
70	75	5	5	72	5	5	74	51	188
80	79	8	5	77	5	5	78	51	188
90	81	8	5	81	5	5	81	51	188
100	81	5	5	80	5	5	81	51	188
110	81	5	5	82	5	5	81	51	189
120	82	8	5	83	5	8	82	51	191
131	82	8	5	84	5	8	83	51	193
142	83	8	8	86	8	8	85	51	195
153	83	8	8	86	8	8	84	51	197
164	82	11	11	85	8	11	83	51	199
176	80	11	11	-	-	-	80	51	201
<u>N3726</u>									
40	112	10	7	92	12	10	102	53	195
60	131	7	7	119	10	10	125	53	195
80	144	5	5	146	7	10	145	53	195
100	156	5	5	172	5	7	164	53	195
120	154	7	7	171	5	7	162	53	195
140	155	7	5	166	7	7	160	53	195
160	152	7	7	159	5	7	156	53	195
183	145	10	7	148	5	5	147	57	188
256	157	8	8	159	6	6	158	72	180
316	169	9	12	-	-	-	169	75	179
344	169	9	12	-	-	-	169	75	179
373	167	15	15	-	-	-	167	75	179
<u>N3769</u>									
20	89	13	10	86	20	10	88	70	149
40	103	10	8	109	13	10	106	70	149
60	112	8	8	119	8	8	116	70	149
80	120	8	8	130	8	10	125	70	149
100	123	5	8	129	5	8	126	70	149
120	124	5	8	122	5	8	123	70	150
141	120	5	5	115	8	8	118	70	152
166	120	8	10	110	8	10	115	70	155
196	122	14	17	-	-	-	122	70	158
364	121	10	10	-	-	-	121	70	167
396	118	10	10	-	-	-	118	70	167
426	113	11	11	-	-	-	113	70	168
<u>U6667</u>									
10	27	5	5	27	7	7	27	89	89
20	43	2	2	47	5	5	45	89	89
30	55	5	5	59	7	5	57	89	89
40	64	2	5	74	5	5	69	89	89

Table 4. continued

Rad. (")	V <sub>rot</sub> <sup>app</sup> km/s	+/-	V <sub>rot</sub> <sup>rec</sup> km/s	+/-	V <sub>rot</sub> <sup>ave</sup> km/s	i (°)	PA (°)
<i>U6667 (cont.)</i>							
50	73	5 5	82	5 5	77	89	89
60	78	5 5	84	5 7	81	89	89
70	82	2 5	87	5 5	84	89	89
80	83	2 5	87	5 5	85	89	89
90	83	5 5	89	5 5	86	89	89
<i>N3877</i>							
10	35	10 10	40	15 15	38	76	37
20	81	10 10	80	15 15	80	76	37
30	129	10 10	113	15 12	121	76	37
40	150	8 8	134	12 12	142	76	37
50	157	8 8	149	10 10	153	76	37
60	161	8 8	159	8 8	160	76	37
70	163	8 8	163	8 8	162	76	37
80	164	8 8	171	5 5	167	76	37
90	163	8 8	174	8 8	169	76	37
100	164	8 8	177	8 5	171	76	37
110	165	8 8	176	8 5	171	76	37
120	165	8 8	174	10 8	170	76	37
130	166	10 10	171	10 10	169	76	37
<i>N3893</i>							
20	140	10 10	150	10 10	145	49	345
40	175	10 10	173	10 10	174	49	345
60	191	10 10	197	10 7	194	49	345
80	192	7 7	189	10 7	191	49	346
101	192	10 8	181	8 8	186	47	351
125	194	8 11	182	8 11	188	45	362
151	190	10 13	184	10 16	187	43	371
176	179	11 15	-	-	179	41	377
198	161	15 12	190	19 19	176	39	379
218	153	12 12	181	24 24	167	37	380
233	148	21 17	-	-	148	36	381
<i>N3917</i>							
10	21	5 5	28	7 5	24	80	257
20	45	5 5	54	7 5	50	80	257
30	69	7 7	78	7 7	74	80	257
40	99	7 5	103	5 7	101	80	257
50	102	5 5	113	5 5	107	80	257
60	108	5 5	122	5 5	115	80	257
70	118	5 5	128	5 7	123	80	257
80	127	5 5	134	5 7	130	80	257
90	133	5 5	134	5 5	134	79	257
100	137	7 5	136	5 5	136	78	257
110	137	7 5	136	5 5	137	77	257
120	137	5 5	136	5 5	136	77	257
130	137	5 5	137	5 5	137	76	257
140	137	5 5	138	5 5	137	75	257
150	137	5 5	-	-	137	75	257
160	138	5 5	-	-	138	74	257
170	137	8 8	-	-	137	73	257
<i>N3949</i>							
10	58	10 10	79	14 14	68	55	298
20	106	10 7	141	7 7	123	55	298
30	138	7 10	152	7 7	145	55	298
40	150	5 7	155	10 12	152	55	298
50	156	7 7	159	7 14	157	55	297
60	161	5 5	161	10 24	161	55	295
70	165	7 7	165	7 34	165	55	294
81	-	-	169	7 44	169	55	293

Table 4. continued

Rad. (")	V <sub>rot</sub> <sup>app</sup> km/s	+/-	V <sub>rot</sub> <sup>rec</sup> km/s	+/-	V <sub>rot</sub> <sup>ave</sup> km/s	i (°)	PA (°)
<i>N3953</i>							
40	178	7 10	184	15 10	181	62	13
60	200	10 10	207	10 7	203	62	13
80	214	7 10	219	7 7	217	62	13
100	218	7 10	227	10 7	223	62	13
120	219	7 7	229	10 7	224	62	13
140	222	7 7	224	10 10	223	62	13
160	229	10 7	218	7 10	224	62	13
175	234	10 7	-	-	234	62	13
180	-	-	215	10 10	215	62	13
<i>N3972</i>							
10	24	5 5	55	10 7	40	77	297
20	68	7 7	78	7 7	73	77	297
30	86	12 10	93	7 7	89	77	297
40	101	10 7	103	5 7	102	77	297
50	111	7 5	110	5 7	110	77	297
60	117	7 5	116	5 7	116	77	297
70	122	5 5	124	7 7	123	77	297
80	129	5 5	131	5 7	130	77	297
86	131	7 7	-	-	131	77	297
90	-	-	134	5 7	134	77	297
100	-	-	134	5 5	134	77	297
<i>U6917</i>							
20	60	5 5	59	5 5	59	56	123
30	71	5 8	72	5 5	71	56	123
40	86	8 5	83	8 5	85	56	123
50	96	8 8	91	5 5	94	56	123
60	98	5 5	97	5 5	98	56	123
70	100	5 5	100	5 5	100	56	123
80	101	8 5	101	5 5	101	56	123
90	105	5 5	102	5 5	103	56	123
100	110	5 5	101	5 8	105	56	123
110	116	7 7	104	5 7	110	57	123
120	-	-	111	5 7	111	60	124
<i>U6923</i>							
11	41	6 9	-	-	41	65	341
23	54	6 6	-	-	54	65	341
34	70	6 6	76	9 6	73	65	341
44	80	6 6	77	6 6	78	65	344
53	-	-	79	5 5	79	65	347
61	-	-	81	5 5	81	65	350
<i>U6930</i>							
20	58	12 10	52	12 12	55	32	39
40	88	10 7	83	12 10	85	32	39
60	94	7 7	94	10 10	94	32	39
80	98	7 7	100	7 7	99	32	39
100	102	7 7	105	7 7	103	32	39
120	105	7 7	109	7 7	107	32	39
140	107	7 7	110	7 7	109	32	39
150	-	-	110	7 7	110	32	39
160	108	7 7	-	-	108	32	39
180	108	7 7	-	-	108	32	39
190	108	7 7	-	-	108	32	39
<i>N3992</i>							
80	253	7 10	244	10 12	249	56	248
120	264	7 10	265	7 12	264	56	248
160	273	7 10	272	7 7	272	56	248
200	274	7 7	268	7 10	271	56	248
240	273	7 7	256	7 7	264	56	248
280	-	-	242	7 7	242	56	248

**Table 4.** continued

Rad. (")	$V_{\text{rot}}^{\text{app}}$ km/s	+/-	$V_{\text{rot}}^{\text{rec}}$ km/s	+/-	$V_{\text{rot}}^{\text{ave}}$ km/s	i (°)	PA (°)
<i>N3992 (cont.)</i>							
320	247	7 7	242	7 7	244	56	248
360	241	7 7	242	10 10	241	56	248
400	237	7 10	-	-	237	56	248
<i>U6940</i>							
10	19	5 5	18	5 5	18	79	315
20	41	5 5	34	5 8	37	79	315
<i>U6962</i>							
10	50	20 15	75	12 10	62	37	359
20	107	10 7	106	10 7	106	37	359
30	129	7 7	126	7 7	128	37	359
40	142	7 7	145	10 7	144	37	359
50	155	7 7	163	10 10	159	37	359
60	171	7 7	-	-	171	37	359
<i>N4010</i>							
0	34	15 15	-34	15 15	0	90	66
10	59	12 10	20	7 7	39	90	66
20	66	7 10	43	7 7	55	90	66
30	69	5 10	62	12 10	66	90	66
40	80	5 5	88	10 7	84	90	66
50	84	5 5	104	12 10	94	90	66
60	96	5 5	113	10 10	104	90	66
70	108	7 5	122	7 7	115	90	66
80	125	7 5	129	7 7	127	90	66
90	128	7 5	131	7 7	129	90	66
100	123	7 5	131	7 7	127	90	66
110	119	7 5	129	7 7	124	90	66
120	119	5 5	125	5 7	122	90	66
<i>U6969</i>							
10	-	-	26	5 7	26	76	330
20	34	5 7	44	7 7	39	76	330
31	46	5 5	58	5 7	52	76	330
41	60	5 5	69	5 7	65	76	330
51	-	-	79	5 5	79	76	330
<i>U6973</i>							
20	162	5 10	179	5 7	170	71	41
30	174	5 7	174	5 7	174	71	41
40	170	5 7	170	5 7	170	71	42
50	170	5 7	170	5 7	170	71	44
61	171	5 7	172	7 7	171	71	45
72	174	5 8	174	8 8	174	71	46
78	-	-	177	10 10	177	71	47
84	178	5 8	-	-	178	71	47
90	180	5 10	-	-	180	71	48
<i>U6983</i>							
20	58	10 10	56	10 7	57	49	270
30	93	7 5	82	7 7	87	49	270
40	87	7 7	97	10 7	92	49	270
50	84	7 7	103	7 7	94	49	270
60	93	5 5	103	7 7	98	49	270
70	94	5 5	105	7 7	100	49	270
80	95	5 5	108	5 5	102	49	270
90	100	7 7	113	5 5	107	49	270
100	105	7 7	112	5 5	108	49	270
110	111	7 7	110	5 5	111	49	270
120	113	7 7	112	5 5	113	49	270
130	111	7 7	110	7 7	111	49	270
140	107	7 7	109	7 10	108	49	270
145	102	10 10	-	-	102	49	270
150	-	-	109	7 10	109	49	270

**Table 4.** continued

Rad. (")	$V_{\text{rot}}^{\text{app}}$ km/s	+/-	$V_{\text{rot}}^{\text{rec}}$ km/s	+/-	$V_{\text{rot}}^{\text{ave}}$ km/s	i (°)	PA (°)
<i>U6983 (cont.)</i>							
160	-	-	108	10 10	108	49	270
170	-	-	108	10 10	108	49	270
180	-	-	109	12 12	109	49	270
<i>N4051</i>							
20	-	-	121	15 15	121	49	310
25	123	15 15	-	-	123	49	310
40	119	12 10	114	12 10	116	49	310
60	146	10 10	133	10 10	140	49	310
80	163	7 10	156	10 10	160	49	310
100	158	7 7	165	7 7	162	49	310
115	-	-	170	7 7	170	49	310
120	154	7 7	-	-	154	49	310
140	153	10 10	-	-	153	49	310
<i>N4085</i>							
10	35	10 5	50	15 10	42	82	256
20	71	7 5	89	10 10	80	82	256
31	110	12 7	113	7 7	112	82	256
41	126	7 5	127	7 7	127	82	256
51	131	7 7	130	7 5	130	82	256
61	134	7 7	133	5 5	133	82	256
71	136	7 7	-	-	136	82	256
<i>N4088</i>							
20	92	15 15	78	20 15	85	69	230
40	138	10 15	135	20 10	136	69	230
60	156	7 12	168	15 10	162	69	230
80	167	7 10	191	10 10	179	69	230
100	177	7 10	187	10 7	182	69	230
120	185	7 12	174	10 10	179	69	230
140	187	7 12	162	7 7	174	69	230
160	185	12 12	158	7 7	171	69	230
180	175	10 10	161	7 7	168	69	230
200	171	7 7	160	10 7	165	69	230
210	-	-	156	10 7	156	69	229
221	171	10 7	-	-	171	69	227
246	174	8 8	-	-	174	69	224
<i>N4100</i>							
20	67	15 15	-	-	67	73	345
30	102	15 20	139	15 7	121	73	345
40	138	12 12	159	10 7	148	73	345
50	164	7 10	173	10 7	168	73	345
60	177	10 7	188	10 7	182	73	345
70	188	7 7	193	7 7	191	73	345
80	193	7 7	195	10 7	194	73	345
90	195	10 7	195	10 7	195	73	345
100	193	5 7	194	7 7	193	73	345
110	192	5 5	192	7 5	192	73	345
120	193	5 5	191	5 5	192	73	345
130	192	5 5	190	7 7	191	73	345
140	188	7 7	189	7 5	189	73	345
150	183	7 10	187	7 5	185	73	345
160	180	7 7	185	5 5	182	73	345
170	175	10 10	183	10 7	179	72	346
180	172	7 10	181	10 7	177	71	346
190	168	10 10	179	10 8	174	71	346
200	-	-	178	10 8	178	70	346
210	-	-	177	8 5	177	70	347
220	160	5 8	178	10 10	169	69	347
230	158	5 8	-	-	158	69	347
241	158	8 8	-	-	158	68	348

**Table 4.** continued

Rad. (")	$V_{\text{rot}}^{\text{app}}$ km/s	+/-	$V_{\text{rot}}^{\text{rec}}$ km/s	+/-	$V_{\text{rot}}^{\text{ave}}$ km/s	i (°)	PA (°)
<i>N4100 (cont.)</i>							
251	158	8 10	- - -	- - -	158	68	348
261	159	10 8	- - -	- - -	159	67	348
<i>N4102</i>							
20	179	12 12	184	12 12	181	56	39
30	177	12 10	181	10 12	179	56	39
40	174	12 10	178	10 10	176	56	39
50	-	- -	178	15 10	178	56	39
<i>N4157</i>							
20	66	18 14	127	23 14	96	82	63
40	142	18 14	173	14 14	157	82	63
60	192	9 14	191	11 14	192	82	63
80	202	7 9	201	11 11	201	82	63
100	198	11 11	204	9 9	201	82	63
120	192	9 9	197	9 9	195	82	63
140	191	9 9	188	9 7	190	82	63
160	191	9 9	181	9 9	186	82	63
180	192	9 9	176	9 9	184	82	63
200	191	9 9	173	11 11	182	82	63
220	190	7 7	173	14 9	181	82	63
240	189	9 7	177	11 9	183	82	63
260	189	11 7	181	9 9	185	82	63
280	186	11 7	- - -	- - -	186	82	63
300	186	11 11	- - -	- - -	186	82	63
320	185	14 14	- - -	- - -	185	82	63
340	185	14 14	- - -	- - -	185	82	63
<i>N4183</i>							
10	56	12 10	38	15 10	47	82	346
20	71	7 7	61	12 10	66	82	346
30	78	7 7	74	10 7	76	82	346
40	88	7 7	84	10 7	86	82	346
50	97	7 7	97	7 7	97	82	346
60	100	7 7	99	7 7	99	82	346
70	103	7 7	103	7 7	103	82	346
80	106	7 7	107	7 7	107	82	346
90	110	7 7	113	7 7	111	82	346
100	112	7 7	117	10 10	114	82	346
110	112	7 7	118	10 10	115	82	346
120	108	7 7	114	10 7	111	82	346
130	108	7 7	113	10 7	110	82	347
141	111	7 7	112	7 7	111	82	347
151	108	7 5	110	7 7	109	82	347
161	106	5 5	109	7 7	108	82	347
172	109	7 7	109	7 7	109	82	347
183	112	7 7	110	7 7	111	82	348
194	108	5 8	111	8 8	110	82	348
205	106	5 8	111	8 8	109	82	348
217	107	7 8	112	8 8	110	82	348
229	-	- -	112	10 10	112	82	348
241	-	- -	113	13 10	113	82	349
<i>N4217</i>							
10	38	10 10	57	14 12	48	86	230
20	82	10 12	116	14 10	99	86	230
30	145	10 10	148	14 10	146	86	230
40	162	7 10	165	10 10	164	86	230
50	176	7 10	172	7 10	174	86	230
60	176	7 10	175	10 7	175	86	230
70	189	7 10	179	10 10	184	86	230
80	188	7 10	182	10 10	185	86	230
90	187	5 10	188	12 10	188	86	230

**Table 4.** continued

Rad. (")	$V_{\text{rot}}^{\text{app}}$ km/s	+/-	$V_{\text{rot}}^{\text{rec}}$ km/s	+/-	$V_{\text{rot}}^{\text{ave}}$ km/s	i (°)	PA (°)
<i>N4217 (cont.)</i>							
100	188	7 10	192	12 12	190	86	230
110	191	7 10	191	10 10	191	86	230
120	192	7 7	189	10 7	191	86	230
130	191	10 7	187	10 7	189	86	230
140	187	10 7	185	12 10	186	86	230
150	183	10 7	183	10 10	183	86	230
160	180	12 7	178	10 10	179	86	230
170	177	10 10	177	10 12	177	86	230
181	178	12 12	177	10 14	177	86	230
191	178	12 12	- - -	- - -	178	86	230
<i>N4389</i>							
10	30	8 8	25	10 8	27	50	277
20	56	10 8	50	13 8	53	50	277
31	70	13 8	69	10 8	69	50	277
41	79	13 8	88	8 8	84	50	277
51	92	10 10	99	8 8	96	50	277
61	-	- -	110	8 8	110	50	277
<i>Rotation curves derived from XV-diagrams only.</i>							
<i>N3718</i>							
40	228	10 10	228	10 10	228	76	114
80	228	10 10	228	10 10	228	80	130
120	228	10 10	228	10 10	228	84	143
160	228	10 10	228	10 10	228	90	162
200	228	10 10	228	10 10	228	85	175
240	220	10 10	235	10 10	228	80	186
280	225	10 10	239	10 10	232	75	195
320	240	10 10	245	10 10	242	70	196
360	245	10 10	242	10 10	244	65	196
400	235	10 10	240	10 10	237	65	194
420	227	10 10	- - -	- - -	-	65	194
<i>N3729</i>							
20	118	34 24	138	12 10	128	48	164
40	157	17 12	141	12 12	149	48	164
50	-	- -	144	10 10	144	48	164
60	151	12 10	- - -	- - -	151	48	164
<i>U6773</i>							
10	28	10 7	34	10 7	31	60	341
20	38	7 7	48	7 5	43	60	341
30	46	5 5	44	7 7	45	60	341
40	47	5 5	44	10 7	45	60	341
<i>U6818</i>							
10	27	7 7	20	10 7	23	79	77
20	28	10 7	28	7 5	28	79	77
30	31	7 5	43	7 5	37	79	77
40	43	7 5	53	7 5	48	79	77
50	66	7 7	61	7 5	63	79	77
60	77	7 10	66	7 5	71	79	77
70	68	7 5	- - -	- - -	68	79	77
80	74	7 5	- - -	- - -	74	79	77
<i>N3985</i>							
0	8	15 10	-8	15 10	0	53	70
10	41	10 7	37	12 7	39	53	70
20	60	7 10	89	15 7	75	53	70
25	68	10 10	- - -	- - -	68	53	70
30	-	- -	93	7 7	93	53	70
<i>U6894</i>							
10	28	7 7	28	12 10	28	89	269
20	45	7 7	45	7 7	45	89	269

**Table 4.** continued

Rad. (")	$V_{\text{rot}}^{\text{app}}$ km/s	+/-	$V_{\text{rot}}^{\text{rec}}$ km/s	+/-	$V_{\text{rot}}^{\text{ave}}$ km/s	i (°)	PA (°)
<i>U6894 (cont.)</i>							
30	56	7 5	56	5 5	56	89	269
40	62	5 5	63	7 7	63	89	269
<i>N4013</i>							
65	-	- -	198	10 10	198	90	245
73	-	- -	195	5 5	195	90	245
82	193	5 5	195	3 3	194	90	245
91	195	4 4	195	3 3	195	90	245
99	195	3 3	195	3 3	195	90	245
108	195	3 3	193	4 4	195	90	245
117	196	3 3	185	5 5	192	90	245
125	195	3 3	178	5 5	188	90	245
134	190	4 4	178	8 8	186	90	245
143	190	4 4	-	- -	186	90	245
151	188	5 5	-	- -	186	90	245
160	187	6 6	-	- -	185	90	245
168	179	10 10	-	- -	180	90	243
177	163	8 8	-	- -	163	90	240
186	161	6 6	-	- -	162	90	238
194	162	5 5	-	- -	164	90	236
203	164	5 5	170	5 5	166	90	235
212	164	6 6	168	5 5	166	90	233
220	165	8 8	166	5 5	166	90	232
229	165	7 7	166	5 5	166	90	230
238	169	5 5	168	5 5	168	90	229
246	173	5 5	-	- -	172	90	228
255	173	5 5	-	- -	173	90	226
264	172	5 5	-	- -	171	90	225
272	169	6 6	170	5 5	170	90	224
281	162	10 10	172	5 5	172	90	224
289	-	- -	174	5 5	173	90	223
298	-	- -	176	5 5	176	90	222
307	-	- -	178	5 5	178	90	221
315	-	- -	180	6 6	180	90	221
324	-	- -	180	8 8	180	90	220
333	-	- -	180	5 5	180	90	219
341	-	- -	180	5 5	180	90	219
350	-	- -	178	5 5	178	90	218
359	-	- -	174	5 5	174	90	218
367	-	- -	170	10 10	170	90	218
<i>U7089</i>							
10	25	7 7	17	7 5	21	89	215
20	38	5 5	35	7 7	36	89	215
30	45	5 5	42	7 7	43	89	215
40	51	7 7	51	5 5	51	89	215
50	57	7 5	62	5 5	60	89	215
60	63	10 5	66	5 5	65	89	215
70	66	7 5	69	5 5	68	89	215
75	-	- -	73	7 7	73	89	215
80	70	7 5	-	- -	70	89	215
<i>U7089 (cont.)</i>							
90	74	7 5	-	- -	74	89	215
100	78	7 5	-	- -	78	89	215
105	79	7 7	-	- -	79	89	215
<i>U7094</i>							
20	32	5 5	32	5 5	32	72	39
40	36	7 5	36	7 5	36	72	39
60	-	- -	35	7 5	35	72	39

**Table 4.** continued

Rad. (")	$V_{\text{rot}}^{\text{app}}$ km/s	+/-	$V_{\text{rot}}^{\text{rec}}$ km/s	+/-	$V_{\text{rot}}^{\text{ave}}$ km/s	i (°)	PA (°)
<i>N4138</i>							
30	178	19 34	181	12 12	179	53	151
60	191	10 10	200	10 10	195	53	151
90	181	10 10	181	15 20	181	53	147
122	-	- -	162	26 15	162	51	143
154	145	14 14	145	14 14	145	48	140
184	-	- -	147	18 18	147	43	138
213	-	- -	150	21 21	150	35	138
<i>N4218</i>							
10	51	10 7	70	12 10	60	55	316
20	83	10 5	62	12 10	73	55	316

Due to the assumed velocity anisotropy,  $W_{t,l}$  has become a function of inclination angle and varies in the range  $45 < W_{t,20} < 57$  and  $17 < W_{t,50} < 21$  for inclinations ranging between  $45^\circ < i < 90^\circ$ .

The same value of  $k_{20}=1.89$  was adopted by TFq but they assumed an isotropic velocity dispersion of  $\sigma_x=\sigma_y=\sigma_z=10$  km/s and consequently advocate  $W_{t,20}=2 \cdot 1.89 \cdot 10=38$  km/s, independent of inclination. They did not address the situation at the 50% level.

Fouqué et al. (1990) also assumed isotropy but adopted  $\sigma=12$  km/s. They determined  $k_l$  in a more direct way by comparing the corrected line width to the observed maximum rotational velocity  $V_{\text{max}}$  as derived from HI velocity fields. They found  $k_{20}=1.96$  and  $k_{50}=1.13$ , indicating a near-Gaussian distribution, contrary to the findings of Bottinelli et al. Consequently, Fouqué et al. advocate the much larger values of  $W_{t,20}=47$  km/s and  $W_{t,50}=27$  km/s respectively.

A similar procedure was followed by Broeils (1992) using a sample of 21 galaxies with well defined HI velocity fields. Broeils made no a priori assumptions about the intrinsic velocity dispersion and did not decouple  $k_l$  and  $\sigma$ . He did, however, recognize that  $V_{\text{max}}$  may exceed  $V_{\text{flat}}$  and he determined for each galaxy the values of  $W_{t,l}^{\text{max}}$  and  $W_{t,l}^{\text{flat}}$  for which the differences

$$\begin{aligned} \Delta W_{R,l}^{\text{max}} &= W_{R,l} - 2V_{\text{max}} \sin(i) \\ \text{and} \\ \Delta W_{R,l}^{\text{flat}} &= W_{R,l} - 2V_{\text{flat}} \sin(i) \end{aligned}$$

become zero for each galaxy. He found mean values of

$$\begin{aligned} W_{t,20}^{\text{max}} &= 21 \pm 2 \quad , \quad W_{t,50}^{\text{max}} = 7 \pm 1 \\ W_{t,20}^{\text{flat}} &= 37 \pm 5 \quad , \quad W_{t,50}^{\text{flat}} = 25 \pm 4 \end{aligned}$$

(Note that he quoted the much larger scatters instead of the errors in the mean quoted above.) He rejected his results, probably discouraged by the large *scatters*, and adopted the values  $W_{t,20}=38$  and  $W_{t,50}=14$  km/s which he erroneously identifies with Bottinelli et al.'s results.

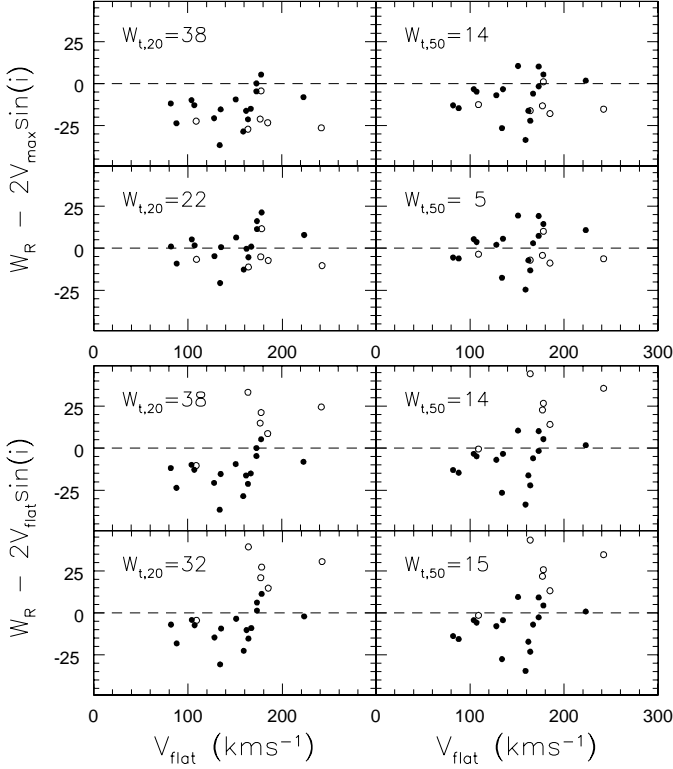


**Fig. 2.** Comparison of the global profile widths  $W_{R,l}$ , corrected for instrumental broadening and random motions, with  $2V_{\max}\sin(i)$  (Upper panels) and with  $2V_{\text{flat}}\sin(i)$  (lower panels). The left panels consider  $W_{R,20}$  and the right panels  $W_{R,50}$ . Different values of the random motion parameters  $W_{t,l}$  are used. Open symbol indicate galaxies with declining rotation curves ( $V_{\max} > V_{\text{flat}}$ ) and filled symbols indicated galaxies without a declining part ( $V_{\max} = V_{\text{flat}}$ ). See section 4 for further details.

Finally, Rhee (1996a) performed the same investigation using 28 galaxies, most of them in common with Broeils’ (1992) sample. Not surprisingly, he found

$$\begin{aligned}
 W_{t,20}^{\max} &= 20 \pm 2 & , & & W_{t,50}^{\max} &= 8 \pm 2 \\
 W_{t,20}^{\text{flat}} &= 30 \pm 3 & , & & W_{t,50}^{\text{flat}} &= 18 \pm 3
 \end{aligned}$$

similar to Broeils’ result.

Here, with our new and independent dataset, we follow the same strategy as Broeils and Rhee by investigating which values of  $W_{t,l}$  allow an accurate retrieval of  $V_{\max}$  and  $V_{\text{flat}}$  from the broadened global profile. For this purpose we will only consider those 22 galaxies in our Ursa Major sample that show a flat part in their rotation curves (with a significant amount of HI gas) and that are free from a major change in inclination angle. Of these 22, there are 6 galaxies with  $V_{\max} > V_{\text{flat}}$ . Note that both Broeils and Rhee used Bottinelli et al.’s prescription to correct for instrumental broadening which we are forced to adopt here to ensure a valid comparison between their

and our results. We calculated the values of  $W_{t,l}^{\max}$  and  $W_{t,l}^{\text{flat}}$  for which the average values

$$\begin{aligned}
 \overline{\Delta W_{R,l}^{\max}} &= \frac{1}{N} \sum (W_{R,l} - 2V_{\max}\sin(i)) \\
 \overline{\Delta W_{R,l}^{\text{flat}}} &= \frac{1}{N} \sum (W_{R,l} - 2V_{\text{flat}}\sin(i))
 \end{aligned}$$

become zero. This is done for both the entire sample of  $N=22$  galaxies and for the subsample of  $N=16$  galaxies with  $V_{\max} = V_{\text{flat}}$ . For the entire sample we find

$$\begin{aligned}
 W_{t,20}^{\max} &= 22 & , & & W_{t,50}^{\max} &= 5 \\
 W_{t,20}^{\text{flat}} &= 32 & , & & W_{t,50}^{\text{flat}} &= 15
 \end{aligned}$$

These values are in good agreement with the (rejected) results of Broeils and in excellent agreement with the results of Rhee. The values of  $W_{t,l}^{\text{flat}}$  are larger than the values of  $W_{t,l}^{\max}$  because the galaxies with  $V_{\max} > V_{\text{flat}}$  in our sample have considerable amounts of HI gas at their peak velocity in the rotation curve. This gas, rotating at  $V_{\max}$  broadens the global profile somewhat further. If we consider only the 16 galaxies for which  $V_{\max} = V_{\text{flat}}$  we find

$$W_{t,20}^{\max} = W_{t,20}^{\text{flat}} = 23 & , & W_{t,50}^{\max} = W_{t,50}^{\text{flat}} = 6$$

in agreement with the values of  $W_{t,l}^{\max}$  we found when using all 22 galaxies.

Our results are illustrated in Figure 2 where we show, for each of the 22 galaxies, the deviations  $\Delta W_{R,l}^{\max}$  (upper panels) and  $\Delta W_{R,l}^{\text{flat}}$  (lower panels) as a function of  $V_{\text{flat}}$ . Galaxies with  $V_{\max} = V_{\text{flat}}$  are indicated by filled symbols, galaxies with  $V_{\max} > V_{\text{flat}}$  are indicated by open symbols. The upper two panels in each block show the results one obtains when using Broeils’ adopted values of  $W_{t,20} = 38$  and  $W_{t,50} = 14$  km/s.

From the upper panels in the upper block it is clear that the maximum rotational velocity as derived from the corrected global profiles is severely underestimated when using the values of  $W_{t,l}$  derived by TFq and adopted by Broeils. This systematic underestimation disappears when  $W_{t,20}$  is decreased from 38 to 22 km/s and  $W_{t,50}$  is decreased from 14 to 5 km/s. The upper two panels in the lower block show that if one is interested in the amplitude of the flat part, which is smaller than the maximum rotational velocity for galaxies with a declining rotation curve (open symbols), the average offset becomes less significant simply because the open symbols scatter upward. In this case, to obtain an average zero offset, we find similar values for  $W_{t,l}$  as those adopted by Broeils. However, we find the curious situation that the corrected width of the global profile systematically overestimates  $V_{\text{flat}}$  for galaxies with a declining rotation curve (open symbols) and systematically underestimates  $V_{\text{flat}}$  for galaxies with a purely flat rotation curve (filled symbols).



From this we can conclude that, in a statistical sense, the maximum rotational velocity of a galaxy can be reasonably well retrieved from the width of the global profile when using  $W_{t,20} = 22$  or  $W_{t,50} = 5$  km/s. The amplitude of the flat part can not be retrieved consistently for a mixed sample containing galaxies with declining rotation curves. Note that we have explored only a restricted range of rotational velocities: 80–200 km/s.

Our results also indicate a non-Gaussian distribution of random velocities in the sense that  $W_{t,20}/W_{t,50} \neq 1.80/1.18$ . Interpreting  $W_{t,20}$  and  $W_{t,50}$  in terms of velocity dispersions it follows that

$$\begin{aligned} \sigma_{20} &= W_{t,20}/2k_{20} = 6.1 \text{ km/s} \\ \sigma_{50} &= W_{t,50}/2k_{50} = 2.1 \text{ km/s} \end{aligned}$$

where  $k_{20}=1.80$  and  $k_{50}=1.18$  for a Gaussian distribution. Recall, however, that we advocate a different correction for instrumental broadening than Bottinelli et al.'s scheme used by Broeils and Rhee. With our correction method for instrumental broadening we find the somewhat smaller values of:

$$W_{t,20} = 22 \quad , \quad W_{t,50} = 2$$

These smaller values of  $W_{t,l}$  allow to retrieve  $V_{\text{flat}}$  from the global profiles of galaxies with purely flat rotation curves and  $V_{\text{max}}$  for galaxies with declining rotation curves. Applying our correction method for instrumental resolution and the above-mentioned value of  $W_{t,20} = 22$  km/s we find an rms scatter in  $\Delta W_{20} = 0.5W_{R}^i - V_{\text{max}}$  of 6.8 km/s.

## 5. A comparison of inclinations

Present day instrumentation allows accurate measurements of the luminosities and global HI profiles of galaxies. In general, the observed scatter in the TF-relation is larger than can be explained by the observational uncertainties in these measured parameters alone. However, the uncertainty in corrections sensitive to inclination contribute significantly to the observed scatter. For a sample of randomly oriented galaxies more inclined than 45 degrees, an uncertainty of 1, 3 or 5 degrees in the inclination angle contributes respectively 0.04, 0.12 or 0.19 magnitudes to the scatter due to the uncertainty in line widths alone, assuming a slope in the TF-relation of  $-10$ . Therefore, it is important to determine the inclination angle of a galaxy as accurate as possible and this issue deserves some special attention.

From the photometric and HI synthesis data available, three independent measurements of the inclination angle of a galaxy can in principle be obtained;  $i_{\text{opt}}$  from the optical axis ratio,  $i_{\text{HI}}$  from the apparent ellipticity of the HI disk, and  $i_{\text{VF}}$  from fitting tilted rings to the HI velocity field. Each of these methods has its own systematic limitations which are important to recognize when estimating

the actual inclination of a galaxy. In the following discussion we will briefly address those limitations and make an intercomparison of  $i_{\text{opt}}$ ,  $i_{\text{HI}}$ , and  $i_{\text{VF}}$ .

### 5.1. $i_{\text{opt}}$ from optical axis ratios

The most widely used formula to infer the inclination angle from the observed optical axis ratio  $(b/a) \equiv q$  was provided by Hubble (1926):

$$\cos^2(i_{\text{opt}}) = \frac{q^2 - q_0^2}{1 - q_0^2}$$

where  $q_0$  is the intrinsic thickness of an oblate stellar disk. Holmberg (1946) determined an average value of  $q_0=0.20$  which is still commonly used although it is obvious from images of edge-on systems that large variations in  $q_0$  exist. For instance, Fouqué et al. (1990) found  $q_0$  to vary from 0.30 to 0.16 for spirals of morphological types Sa to Sd respectively and  $q_0=0.42$  for galaxies of type Sdm-Im. Apart from the debate on the intrinsic thickness, the observed axis ratio  $q$  itself has limited meaning since it is often defined at a certain isophote around which  $q$  may still vary as a function of radius. From images of edge-on disks in the Ursa major cluster (see Paper I) it can often be observed that the axis ratio keeps increasing outward until the faintest isophotes. An extreme example is NGC 4389, dominated by a narrow bar and surrounded by an extended faint halo. The axis ratios presented in Table 1 were not determined at a fixed isophote but were chosen to represent the stellar disk instead of a bulge, lopsided structures or a faint halo.

### 5.2. $i_{\text{HI}}$ from the inclined HI disk

Apart from the oblate stellar disk, the HI disk can also be used to determine the inclination. In general, the HI disk is much thinner than the stellar disk and its intrinsic thickness is of no concern. However, its patchiness, lopsidedness and the existence of warps and tidal tails may complicate the interpretation of the results from fitting ellipses to a certain HI isophote. Here, no correction for the intrinsic thickness of the HI layer was applied. However, the relatively large synthesized beams of imaging arrays at 21cm may smear the observed HI disks to a rounder appearance. Therefore, a simple correction for beam smearing was applied to our measurements and the inclination of the HI disk was determined according to

$$\cos^2(i_{\text{HI}}) = \frac{d_{\text{HI}}^2 - \Theta_{\text{d}}^2}{D_{\text{HI}}^2 - \Theta_{\text{D}}^2}$$

where  $D_{\text{HI}}$  and  $d_{\text{HI}}$  are the observed major and minor axis diameters of the inclined HI disk obtained by fitting an ellipse to the outer column density levels.  $\Theta_{\text{D}}$  and  $\Theta_{\text{d}}$  are the sizes of the synthesized beam in the direction of the major and minor axis of the HI disk.

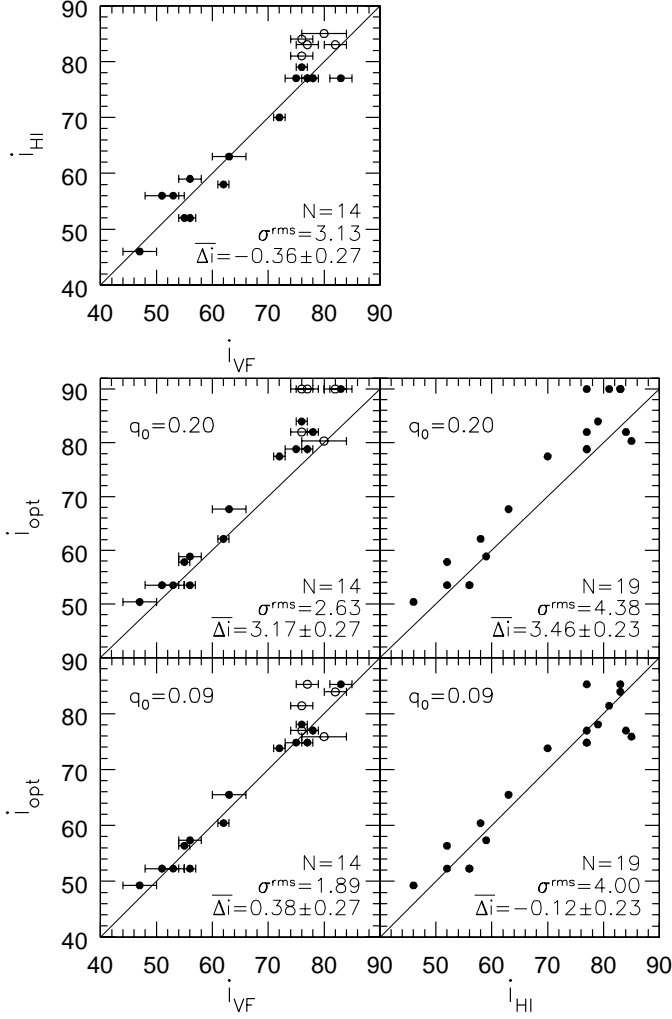


**Fig. 3.** Intercomparison of the three independently determined inclination angles  $i_{opt}$ ,  $i_{HI}$  and  $i_{VF}$ . Only the filled symbols ( $i_{HI} < 80^\circ$  when  $i_{VF}$  is involved) are considered for the unweighted quantitative assessment.

5.3.  $i_{VF}$  from HI velocity fields

The inclination angle of an HI disk can also be measured by fitting tilted-rings to its velocity field (Begeman 1989). However, the inclination angle and the rotational velocity are strongly coupled and reasonable results can only be obtained for inclination angles between roughly 50 and 75 degrees. This procedure requires accurate velocity fields with high signal-to-noise ratios as well as many independent points along a ring. The advantage that velocity fields offer is the possibility to identify warps and to check the kinematic regularity of the HI disk. For instance, the optical appearance of a galaxy may look very regular while the outer regions of the HI disk may be strongly warped toward edge-on (e.g N3726). Such a warp would broaden the global profile and an inclination correction based on the optical axis ratio would lead to an overestimate of the ro-

tational velocity when dividing the ‘warp-broadened’ line width by  $\sin(i_{opt})$ .

Note that the inclination measurement of a tilted ring may be affected by non-circular motions due to spiral arms, bars and lopsidedness.

5.4. the comparison

For the comparison between the three differently inferred inclination angles we considered only those 27 galaxies with fully reduced HI data for which the velocity fields and integrated HI maps are available. We excluded the interacting galaxies (N3769, N3893, U6973) because their outer isophotes (optical and HI) are affected by tidal tails. We also excluded galaxies with perturbed or inadequately sampled velocity fields (N4088, U6969, N4389), galaxies with excessively patchy HI maps (N4102) and obviously lopsided galaxies (N4051). These eliminations leave us with 19 galaxies that have smooth outer isophotes, well filled HI disks and regular HI velocity fields.

Figure 3 presents the comparison between the three differently inferred inclination angles using two different values for  $q_0$ . When calculating mean differences and scatters using  $i_{VF}$ , only galaxies with  $i_{HI} < 80^\circ$  are considered because kinematic inclinations of highly inclined galaxies are systematically underestimated. The error bars on  $i_{VF}$  are based on the variations in  $i_{VF}$  between the various fitted rings but are not considered any further here.

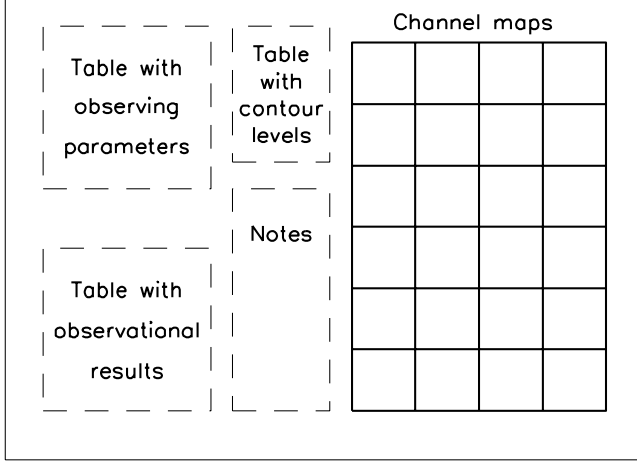
The upper most panel compares  $i_{VF}$  with  $i_{HI}$ . No significant offset is found for the 14 galaxies that meet the above-mentioned criteria. Assuming that  $i_{VF}$  and  $i_{HI}$  contribute equally to the scatter of 3.1 degrees implies that the inclination angle can be determined with an accuracy of 2.2 degrees from either the velocity fields or from the inclined HI disk. Note that the correlation turns up for  $i_{HI} > 80^\circ$  due to the systematic underestimation of  $i_{VF}$  for highly inclined disks.

Comparing  $i_{opt}$  with  $i_{VF}$  and  $i_{HI}$  does show a significant offset of roughly 3 degrees when assuming  $q_0=0.20$  (middle panels). This offset is biggest toward edge-on as would be expected in case of an overestimate of the intrinsic thickness. Note that there are several galaxies with an observed optical axis ratio less than 0.20 which have been assigned an inclination angle of  $90^\circ$ .

This  $3^\circ$  offset disappears when  $q_0=0.09$  is used (lower panels) and the rms scatter is reduced to only 1.9 degrees for  $i_{opt}$  versus  $i_{VF}$  but is still 4.0 degrees in case of  $i_{opt}$  versus  $i_{HI}$ . In the latter case, the scatter is caused by a few nearly edge-on systems for which the higher uncertainties have no influence on the deprojection of the rotational velocities.

The adopted inclinations and their errors, listed in column 11 of Table 1 are best estimates based on all the information available for a particular galaxy, including the morphology of dust lanes if present. For galaxies which

## First page



## Second page

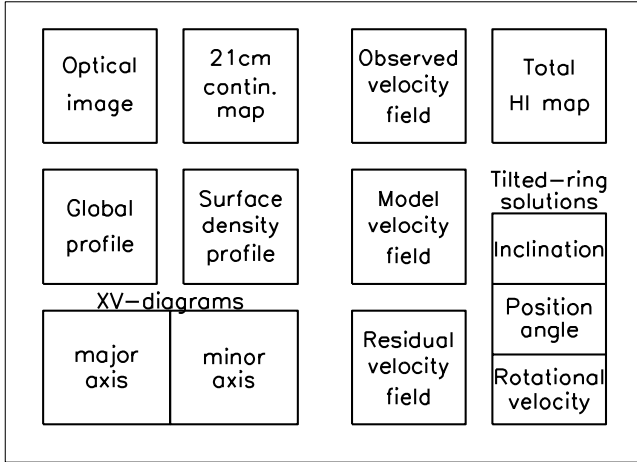


**Fig. 4.** Layout of the HI atlas pages for the 30 galaxies with fully reduced data. All the data for these galaxies are presented on two facing pages. Results for the 13 galaxies with partially reduced data are presented on a single page per galaxy and include only the channel maps, the global profile and the XV-diagram. The linear scale is 5.4 kpc per arcminute.

lack fully reduced HI synthesis data, the inclination angles were inferred from the optical axis ratios using  $q_0=0.09$  for galaxies of type Sc and later and  $q_0=0.24$  for galaxies of type Sbc and earlier. The latter value of  $q_0$  seemed justified by the observed axis ratios of the (nearly) edge-on systems N4013, N4026 and N4111 of types Sb, S0 and S0 respectively. Unfortunately, there are not enough suitable galaxies available to determine  $q_0$  as a function of morphology.

## 6. The atlas

The atlas is presented in Appendix B and consists of two parts. The first part presents the data for the 30 galaxies which have been fully reduced and analyzed. The second part gives a less elaborate presentation of the remaining 13 galaxies which have been only partially reduced.

The reduction procedures described in Section 3 were applied to the data at all three angular resolutions. However, to facilitate the intercomparison of various results for a galaxy, it was decided to present the data of a particular galaxy at the same angular resolution as much as possible. The rotation curves are in some cases a combination of the rotation curves at various resolutions, the inner parts at the highest spatial resolution and the outer parts from data of lower resolution but higher signal-to-noise ratio. The channel maps are sometimes presented at a lower angular resolution than the other data.

Figure 4 shows the graphical layout for each of the 30 galaxies in the first part of the atlas. The data for each of the 13 galaxies in the second part of the atlas are presented on a single page which contains the tables and notes as well as the mosaic of channel maps, the global profile and the XV-diagram along the major axis. The contents of the various tables and panels are described below.

**Tables and Notes** – There are three tables presented for each galaxy. The upper left table contains information on the observations like date, integration time and correlator settings. The lower left table presents some of the quantities derived from the HI data like global profile widths, integrated HI flux, systemic velocity etc. The upper right table provides the noise and contour levels for the maps in the various panels. The contours in the channel maps, 21cm continuum maps and XV-diagrams are always drawn at levels which are related to the rms noise.

The notes contain information about specific aspects of a particular galaxy like optical and HI appearance.

**Channel maps** – The channel maps show how the HI emission behaves as a function of velocity. From these maps it is possible to recognize the presence of warps, non-circular motions and HI-bridges between interacting galaxies like N3769/1135+48 and N3893/N3896. The contours are drawn at levels of -3, -1.5 (dashed), 1.5, 3, 4.5, 6, 9, 12, 15, ... $\sigma$ . The value of the rms noise level  $\sigma$  is given in the upper right table. In each panel, the cross indicates the adopted dynamical center of the galaxy. The ellipse in the upper left panel is centered on this position and the position angle is set at the kinematic major axis of the inner regions. The ellipticity represents the inclination as derived from the optical axis ratio and the major axis diameter is equal to  $D_{25}^{b,i}$ . The synthesized beam at half power is shown in the lower left corners of the left panels. The panel at the lower right shows the subtracted, ‘dirty’ continuum map.

**Optical image** – The optical image of a galaxy was scanned from the blue POSS plates. In the upper left cor-

ner, the morphological type according to the RC3 is given. CCD images of far superior quality can be found in Paper I. An example is given for N3726 in which case the CCD image is pasted into the POSS image.

**Radio continuum map** – The cleaned 21cm radio continuum map is plotted at the same scale as the optical image. The contours are drawn at levels of -4, -2 (dashed), 2, 4, 8, 16, 32, 64,... $\sigma$ . The value of the rms noise  $\sigma$  is given in the upper right table. The ellipse represents the optical image as in the upper left panel in the channels maps. The synthesized beam is plotted in the lower left corner and the small cross indicates the adopted position of the center of rotation.

**Global profile** – Each point in the global HI profile gives the primary-beam corrected, total HI flux density integrated over a single channel map. The errors are derived as explained in Section 3.2. The vertical arrow indicates the systemic velocity (lower left table on the first page) as derived from the HI velocity field and does not necessarily indicate the center of the global HI profile. A significant offset from the center could indicate non-circular motions or a strong lopsidedness. These anomalies can often be traced in the individual channel maps.

**Surface density profile** – The open and filled symbols indicate the azimuthally averaged radial surface densities for the approaching and receding sides. The solid line follows the average value. At the adopted distance of 18.6 Mpc, 1 arcmin corresponds to 5.4 kpc. The vertical arrow indicates  $R_{25}^{b,i}$ . The profile becomes unreliable for highly inclined systems since no correction for beam smearing was applied.

**XV-diagrams** – The position-velocity diagrams are shown for two orthogonal cuts through the adopted center of rotation along the kinematic major (left) and minor (right) axes. The position angles of these two axes are printed in the upper right corner of each panel. Note that the quoted position angles refer to the positive offset axes. Consequently, the position angle of the major axis refers to the receding side which also can be inferred from the channel maps. The vertical dashed line indicates the position of the center of rotation. The horizontal dashed line indicates the systemic velocity as derived from either the velocity field for galaxies with fully reduced data, or from the XV-diagram for galaxies in the second part of the atlas. The two vertical arrows show where the ellipse with major axis diameter  $D_{25}^{b,i}$  intersects the XV-slice. The horizontal arrows in the left panel show the systemic velocity  $V_{\text{sys}}^{\text{GP}}$  derived from the global profile and  $V_{\text{sys}}^{\text{GP}} \pm \frac{1}{2}W_{R,I}$  where  $W_{R,I}$  is the width of the global profile at the 20% level of peak flux, corrected for instrumental broadening (see section 3.2) and turbulent motions according to TFq.

Contours are at levels of -3, -1.5 (dashed), 1.5, 3, 4.5, 6, 9, 12, 15,... $\sigma$ . The value of the rms noise  $\sigma$  is given in the upper right table. The cross in the lower left corners indicates the angular and velocity resolutions. An offset

of 1 arcmin corresponds to a projected distance of 5.4 kpc from the center.

The crosses give the projected rotational velocities as derived from the tilted rings fit. In some cases, at large radii, a cross can be found without any underlying signal in the XV-diagram. In such cases, the rotational velocity at that radius is defined by points in the velocity field away from the major axis. The open and filled circles indicate the projected rotational velocity estimated directly from these XV-diagrams. These points must be deprojected using the appropriate inclination and position angles to obtain the actual rotation curve for both halves of the galaxy.

**Total HI map** – All pixels in the total HI map with a positive signal have a greyscale value assigned. Because the signal-to-noise ratio along a contour is not constant, the ‘ $3\sigma$ -contour’ is not defined. Section 3.3 and the appendix explain why and how the noise varies across an integrated HI map.

The second contour in the total HI maps corresponds to the *average* value of all pixels with a signal-to-noise ratio between 2.75 and 3.25 and this contour can thus be considered as a pseudo  $3\sigma$ -contour. Wherever a contour goes through an area with  $(\frac{S}{N}) < 3$ , the contour is plotted much thinner. Consequently, the lowest contour, plotted at the ‘ $1.5\sigma$ ’ level, is plotted thin over most of its stretch. The various contour levels in atoms  $\text{cm}^{-2}$  are given in the upper right table. The size of the synthesized beam is plotted in the lower left corner. The beamwidths are the same as in the channel maps unless specified otherwise in the note. The small cross indicates the adopted position of the center of rotation (1 arcmin corresponds to 5.4 kpc).

**Velocity fields** – The greyscales indicate the pixels where a radial velocity was measured. Darker greyscales and white isovelocity contours indicate the receding side. The thick first black contour adjacent to the white ones indicates the adopted systemic velocity. In the ideal case of circular motion and no noise, this thick contour should be a straight line through the center and coinciding with the kinematic minor axis of the galaxy. The isovelocity contours are plotted with constant velocity intervals as given by the upper right table. The synthesized beam is plotted in the lower left corner.

The observed velocity field was modeled by fitting tilted rings to it. The orientation and rotational velocity of each ring were then used to construct the model velocity field. The model velocity field is plotted with the same orientation and on the same scale as the observed velocity field. The isovelocity contours are plotted at the same velocities in the observed as in the model velocity fields. For nearly edge-on systems, the model velocity field is only one or two pixels wide in which case no contours could be drawn.

The residual velocity field was made by subtracting the model from the observed velocity field. White contours indicate positive residuals, black contours indicate negative

residuals. The contour levels are ..., -15, -10, -5, 5, 10, 15, ...  $\text{km s}^{-1}$ .

**Tilted-ring fits** – The three combined panels show the results from the tilted-ring fits to the observed velocity field. The upper panel shows the inclination angle, the middle panel the position angle and the lower panel the rotational velocity.

The crosses with errorbars in the panels for inclination and position angle are the results from the second step of the fitting procedure as explained in section 3.6.1. The dashed lines, mostly coinciding with the solid lines,

Table 5. Results from the HI synthesis observations.

Name	$W_{20} \pm$		$W_{50} \pm$		Res.	$V_{\text{hel}} \pm$		$\int \text{Sdv} \pm$		$F_L \pm$		$R_{\text{HI}}$	$R^{\text{Imp}}$	$V_{\text{rot}}^{\text{Imp}} \pm$		shape	$V_{\text{max}} \pm$		$V_{\text{flat}} \pm$	
(1)	(2)	(3)	(4)	(5)	(6)	(7)	(8)	(9)	(10)	(11)	(12)	(13)	(14)	(15)	(16)	(17)	(18)	(19)	(20)	(21)
<i>Galaxies with fully reduced HI data:</i>																				
U6399	188.1	1.4	172.5	2.9	8.3	791.5	0.6	10.5	0.3	<2.5		1.68	1.50	88	5	R/F	88	5	88	5
U6446	154.1	1.0	131.9	1.2	5.0	644.3	0.8	40.6	0.5	<7.2		2.96	2.93	80	11	F L	82	4	82	4
N3726	286.5	1.6	260.6	1.8	5.0	865.6	0.9	89.8	0.8	49.7	5.0	4.24	6.22	167	15	F/(D)	162	9	162	9
N3769	265.3	6.7	230.5	3.6	8.3	737.3	1.8	62.3	0.6	12.1	2.9	4.31	7.10	113	11	F/(D)	122	8	122	8
U6667	187.5	1.4	178.1	1.9	5.0	973.2	1.2	11.0	0.4	<2.7		1.64	1.50	86	3	R L	86	3	86	3
N3877	373.4	5.0	344.5	6.2	33.2	895.4	3.8	19.5	0.6	35.6	2.4	2.19	2.17	169	7	F L	167	11	167	11
N3893	310.9	1.0	277.9	4.1	5.0	967.2	1.0	69.9	0.5	137.4	2.9	3.98	3.88	148	19	F/(D)	188	11	188	11
N3917	294.5	1.9	279.1	2.1	8.3	964.6	1.4	24.9	0.6	<7.2		2.69	2.83	137	8	F	135	3	135	3
N3949	286.5	1.4	258.3	1.7	8.3	800.2	1.2	44.8	0.4	134.1	3.6	2.62	1.35	169	8	F L	164	7	164	7
N3953	441.9	2.4	413.9	3.2	33.1	1052.3	2.0	39.3	0.8	50.9	2.5	3.32	3.00	215	10	F	223	5	223	5
N3972	281.2	1.4	260.7	5.5	8.3	852.2	1.4	16.6	0.4	<5.8		1.92	1.67	134	5	R L	134	5	...	..
U6917	208.9	3.2	189.6	1.6	8.3	910.7	1.4	26.2	0.3	<4.4		2.42	2.00	111	7	R/F	104	4	104	4
U6923	166.8	2.4	147.1	4.5	10.0	1061.6	2.2	10.7	0.6	<2.6		1.29	1.02	81	5	R L	81	5	...	..
U6930	136.5	0.5	122.1	0.7	8.3	777.2	0.4	42.7	0.3	<5.8		3.20	3.17	108	7	R/F	107	4	107	4
N3992	478.5	1.4	461.4	2.4	10.0	1048.2	1.2	74.6	1.5	30.2	7.6	4.75	6.67	237	9	F/D	272	6	242	5
U6940	59.3	3.8	40.6	7.8	10.0	1118.0	1.7	2.1	0.3	<1.3		0.61	0.33	37	4	R	37	4	...	..
U6962	220.3	6.6	182.4	3.7	8.3	807.4	3.2	10.0	0.3	13.4	1.7	1.38	1.00	171	7	R L	171	7	...	..
N4010	277.7	1.0	264.1	1.2	8.3	901.9	0.8	38.2	0.3	16.9	1.6	3.36	2.00	122	2	(R)/F L	128	9	128	9
U6969	132.1	6.4	123.5	2.9	10.0	1118.5	2.4	6.1	0.5	<3.8		0.95	0.85	79	5	R	79	5	...	..
U6973	367.8	1.8	350.4	1.2	8.3	700.5	1.0	22.9	0.2	127.5	2.1	2.21	1.50	180	8	F/(D)	173	10	173	10
U6983	188.4	1.3	173.0	1.1	5.0	1081.9	0.8	38.5	0.6	<5.4		3.07	3.00	109	12	F	107	7	107	7
N4051	255.4	1.8	224.6	1.5	5.0	700.3	1.2	35.6	0.8	26.5	2.6	2.89	2.33	153	10	R/F L	159	13	159	13
N4085	277.4	6.6	255.4	7.8	19.8	745.7	5.0	14.6	0.9	44.1	1.3	1.94	1.18	136	7	R/F L	134	6	134	6
N4088	371.4	1.7	342.1	1.9	19.8	756.7	1.2	102.9	1.1	222.3	1.9	4.25	4.10	174	8	F/(D) L	173	14	173	14
N4100	401.8	2.0	380.5	1.8	19.9	1074.4	1.3	41.6	0.7	54.3	1.7	3.45	4.35	159	9	F/D	195	7	164	13
N4102	349.8	2.0	322.4	8.5	8.3	846.3	2.0	8.0	0.2	276.0	1.5	1.16	0.83	178	12	F	178	11	178	11
N4157	427.6	2.2	400.7	3.1	19.9	774.4	1.8	107.4	1.6	179.6	2.3	4.60	5.67	185	14	F/D	201	7	185	10
N4183	249.6	1.2	232.5	1.5	8.3	930.1	1.0	48.9	0.7	<5.8		3.07	4.02	113	11	F/D L	115	6	109	4
N4217	428.1	5.1	395.6	3.8	33.2	1027.0	3.0	33.8	0.7	115.6	2.2	3.19	3.17	178	12	F/D	191	6	178	5
N4389	184.0	1.5	164.9	1.6	8.3	718.4	1.2	7.6	0.2	23.3	1.2	1.30	1.02	110	8	R	110	8	...	..
<i>Galaxies with partially reduced HI data:</i>																				
N3718	492.8	1.0	465.7	1.0	33.2	993.0	0.8	140.9	0.9	11.4	0.4		6.67	223	12	F	232	11	232	11
N3729	270.8	1.5	253.2	3.9	33.2	1059.8	1.4	5.5	0.3	18.0	0.9		1.00	151	11	F	151	11	151	11
U6773	110.4	2.3	91.1	2.2	8.3	923.6	1.6	5.6	0.4	<2.6			0.67	45	5	R L	45	5	...	..
U6818	166.9	2.3	141.9	5.7	8.3	808.1	2.1	13.9	0.2	2.4	1.0		1.33	74	7	R/(F) L	73	5	73	5
U6894	141.8	1.1	132.2	1.5	8.3	848.6	1.8	5.8	0.2	<2.7			0.67	63	5	R	63	5	...	..
N3985	160.2	3.7	88.0	2.4	8.3	948.2	2.0	15.7	0.6	9.7	1.4		0.50	93	7	R	93	7	...	..
N4013	425.0	0.9	395.0	0.8	33.0	831.3	0.6	41.5	0.2	36.3	0.8		6.12	170	10	F/D	195	3	177	6
U7089	156.7	1.7	97.7	3.0	10.0	770.0	1.5	17.0	0.6	<3.4			1.75	79	7	R L	79	7	...	..
U7094	83.7	1.7	71.9	5.5	10.0	779.6	1.6	2.9	0.2	<2.6			1.00	35	6	R L	35	6	...	..
N4117	289.4	7.5	260.3	5.2	10.0	934.0	1.5	6.9	1.1	3.7	1.2					?				
N4138	331.6	4.5	266.0	7.8	19.9	893.8	3.9	19.2	0.7	16.7	4.6		3.55	150	21	F/D	195	7	147	12
N4218	138.0	5.0	79.9	1.9	8.3	729.9	1.7	7.8	0.2	6.3	0.8		0.33	73	7	R	73	7	...	..
N4220	438.1	1.3	423.3	3.3	33.1	914.2	1.2	4.4	0.3	<4.9						?				

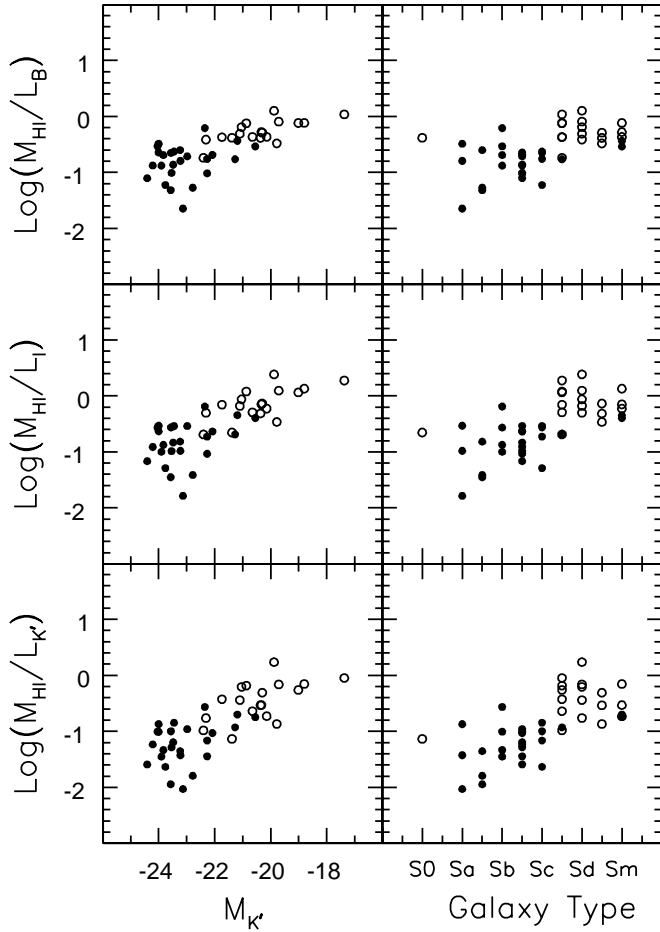


**Fig. 5.** Correlations between HI mass-to-light ratios and absolute  $K'$ -band magnitudes (left column) and morphological type (right column). Solid symbols indicate HSB galaxies and open symbols denote galaxies of the LSB type.

in these upper two panels indicate the final values of the inclination and position angles kept fixed when the rotational velocity was fitted. The resulting rotation curve is shown by crosses with errorbars in the lower panel. The errorbars indicate the formal errors, as given by the least squares minimization algorithm.

The horizontal arrows in the upper two panels indicate the inclination and position angles as derived from the optical isophotes in the outer regions. The diamonds indicate the inclination and position angles as determined from the total HI maps. When the total HI maps are very patchy, these diamonds are very uncertain. The horizontal arrow in the lower panel indicates the rotational velocity as derived from the width of the global HI profile corrected for instrumental broadening, turbulent motion and inclination. The adopted inclination is representative for the outer parts. The vertical arrow in the lower panel indicates  $R_{25}^{b,i}$ .

The solid lines in the upper and middle panels show the inclination and position angles that were adopted to deproject the radial velocities determined from the XV-diagrams. This deprojection results in the rotation curves plotted as open and filled circles in the lower panel (same symbols as in the XV-diagrams). Note that although the rotational velocities at a certain radius may be different for the approaching and receding sides, both sides were assumed to have the same inclination and position angles at that radius. The solid line in the lower panel shows the mean rotation curve derived from the XV-diagram. 1 arcmin on the horizontal axis corresponds to 5.4 kpc.

**Tabulated data** – The various parameters derived from the HI data presented here are summarized in Table 5.

*Column* (1) gives the NGC or UGC numbers.

*Columns* (2)-(5) give the uncorrected widths with formal errors of the global profiles at 20% and 50% of the peak flux.

*Column* (6) gives the instrumental velocity resolution at which the global profiles were observed.

*Columns* (7) and 8 contain the heliocentric systemic velocities and their uncertainties as derived from the global profiles.

*Columns* (9) and (10) provide the integrated HI flux and the uncertainty in  $\text{Jy km s}^{-1}$ .

*Columns* (11) and (12) contain the 21cm continuum flux density and its uncertainty in mJy. In case no continuum flux was detected, a  $3\sigma$  upper limit for extended emission is given.

*Column* (13) gives the radius of the HI disk,  $R_{\text{HI}}$  in arcmin, at the azimuthally averaged surface density of  $1 M_{\odot} \text{pc}^{-2}$ , measured from the radial surface density profiles.

*Column* (14) gives the radius  $R^{\text{lmp}}$  of the last measured point of the rotation curve in arcmin. The differences between  $R^{\text{lmp}}$  and  $R_{\text{HI}}$  depend on the sensitivity of the measurement and the distribution of the HI gas along the kinematic major axis.

*Columns* (15) and (16) give the rotational velocity of the last measured point  $V^{\text{lmp}}$  and its uncertainty.

*Column* (17) contains information on the overall shape of the rotation curve; R: rising rotation curve, F: the rotation curve shows a flat part, D: the rotation curve shows a declining part, L: lopsided.

*Columns* (18) and (19) give the maximum observed rotational velocity  $V_{\text{max}}$  and its uncertainty. For galaxies with a rising rotation curve (R)  $V_{\text{max}} = V^{\text{lmp}}$ .

*Columns* (20) and (21) give the average rotational velocity of the flat part of the rotation curve  $V_{\text{flat}}$  and its uncertainty. For galaxies with a flat rotation curve (F)  $V_{\text{flat}} = V_{\text{max}}$  may deviate from  $V^{\text{lmp}}$  because  $V_{\text{flat}}$  was averaged over the flat part of the rotation curve while  $V^{\text{lmp}}$  was measured at a single point.

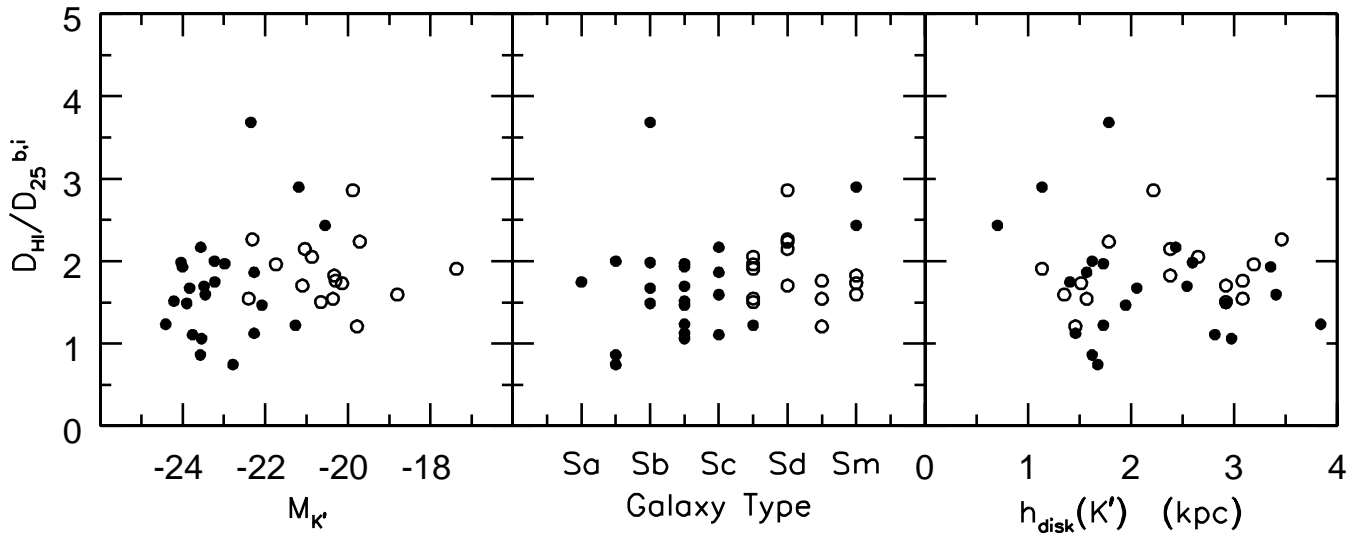


**Fig. 6.** Ratio of HI-to-optical diameter as a function of  $K'$  magnitudes, morphological type and disk scale length. The HI diameters were measured at the  $1 \text{ M}_{\odot} \text{pc}^{-2}$  isodensity contour. Solid symbols indicate HSB galaxies and open symbols denote galaxies of the LSB type.

## 7. HI properties of spirals

The HI survey of the Ursa Major cluster presented here provides not only the kinematical information necessary for the study of the Tully-Fisher relation and of the dark and luminous matter for a well defined sample of galaxies. It also serves to investigate the general HI properties of disks and to make a comparison with galaxies in the field and with galaxies in denser environments. The HI studies of the Virgo cluster galaxies by Warmels (1988a, 1988b) and especially by Cayatte et al. (1990) have shown that the spiral galaxies in the central parts of the cluster have smaller HI disks of lower surface density. In the Hydra Cluster McMahan (1993) did not find any such significant HI deficiency. She did find, however, a surprisingly large number of isolated HI-rich dwarf galaxies near the center of the cluster. Dickey (1997) surveyed the more distant Hercules SuperCluster and found a similar HI deficiency of spirals near the X-ray gas as in the case of Virgo.

The Ursa Major cluster differs from those just mentioned. It has no central concentration, no X-ray emitting gas and contains mainly spirals of late morphological types. In many respects its conditions are very similar to those of a field environment. For this reason it is useful to compare the properties of the Ursa Major spirals not only with those of galaxies in dense cluster environments but also with those of field galaxies as found in various recent studies (see e.g. Broeils 1992, Puche & Carignan 1991, Rhee 1996a, Swaters 1999).

Here we give only a brief description of the global parameters and of the main properties of the HI disks of the Ursa Major galaxies. A more detailed discussion and a comparison with results from previous work is beyond the scope of this data paper.

### 7.1. Global parameters

Integral properties and global parameters of spiral galaxies have been derived for a large number of objects from single-dish observations (cf. Roberts and Haynes 1994). In recent years also synthesis observations (Broeils 1992, Rhee 1996a) have been used to obtain similar information for smaller samples of galaxies.

The  $M_{\text{HI}}/L$  ratios obtained for the galaxies of the Ursa Major sample listed in Table 5 are shown here in Figure 5 as a function of absolute magnitude and of morphological type. It is well known (see refs. above) that the  $M_{\text{HI}}/L$  ratio of galaxies depends on luminosity and morphological type. The present sample of galaxies shows a clear increase of the HI mass fraction with decreasing luminosity and from early to late morphological types. The correlation is clearly stronger for the  $K'$ -band magnitudes which is a better tracer of the stellar mass.

### 7.2. Sizes of HI disks and radial surface density profiles

Detailed information on the sizes and radial distributions of HI disks has been obtained recently from synthesis observations of limited samples of field and cluster galaxies (Broeils and Van Woerden 1994, Cayatte et al. 1994, Rhee 1996a and 1996b). Here we present only some of the main results on the comparison of HI and optical diameters, on the relation between HI mass and diameter and on the radial density profiles for the Ursa Major sample.

Figure 6 shows the ratio of the HI diameter  $D_{\text{HI}}$  (defined at an HI surface density of  $1 \text{ M}_{\odot} \text{pc}^{-2}$ ) to the optical diameter  $D_{25}^{b,i}$  as a function of luminosity, morphological type and disk scale-length. The diagrams do not indicate any clear trend or dependence of the diameter ratio on



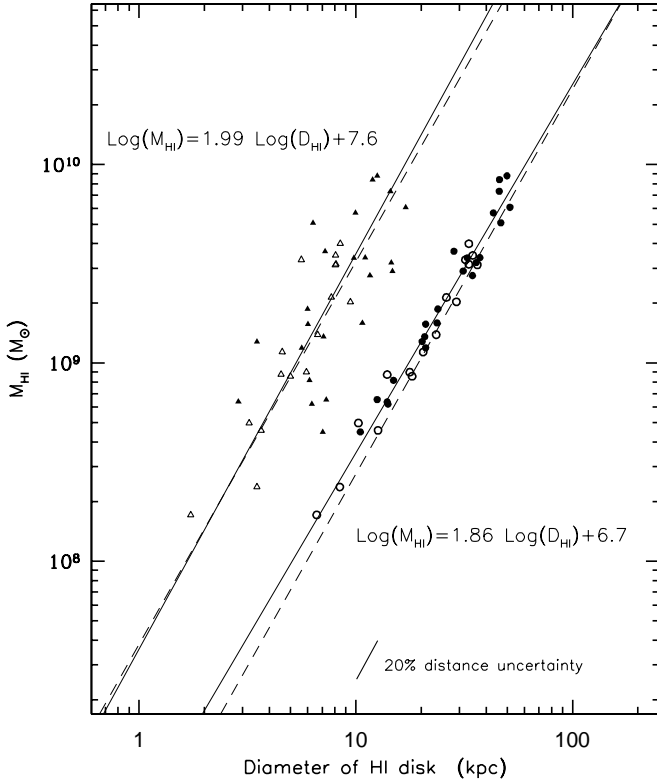


**Fig. 7.** Correlations between HI mass and the isophotal diameters of the stellar (triangles) and HI disks (circles). Solid lines indicate fits to the plotted data points while the dashed lines represent the fits found by Broeils (1992). Filled symbols indicate HSB galaxies and open symbols denote galaxies of the LSB type. Triangles are offset by 0.3 dex to the left.

any of those quantities. The spread is large. There may be a hint of a slight increase of the ratio from early to later types and from more luminous to less luminous systems. For almost all galaxies  $D_{\text{HI}}$  is larger than  $D_{25}^{b,i}$ .

As shown in previous investigations (see refs. above), there is a tight correlation between HI mass and HI diameter as illustrated in Figure 7. This implies a nearly constant mean HI surface density regardless of size. The HI mass correlates also with the optical diameter, but, as in previous work, with a much larger scatter.

### 7.3. Warps, asymmetries and interactions

The radial distributions of the HI surface densities are shown in Figure 8. Only galaxies with fully reduced data, more inclined than 80 degrees and with  $R_{\text{HI}} < 1$  arcmin are considered in order to avoid the most severe cases of beam smearing. There is clearly a considerable diversity of shapes and intensities. The upper row shows the profiles grouped for galaxies of similar morphological types. The dotted lines represent low surface brightness galaxies. No obvious trend with morphological type or surface

**Table 6.** Warps, asymmetries and interactions.

Name	Type	Warped	Lopsided HI distr.	HI kin.	Inter- acting
U6399	Sm		×		
U6446	Sd			×	
N3718	Sa	×			
N3726	SBc	×			
N3729	SBab				
N3769	SBb	×			×
U6667	Scd			×	
N3877	Sc			×	
U6773	Sm			×	
N3893	Sc				×
N3917	Scd		×		
U6818	Sd			×	
N3949	Sbc		×	×	
N3953	SBbc				
U6894	Scd				
N3972	Sbc			×	
U6917	SBd	×			
N3985	Sm	×			
U6923	Sdm	×		×	
U6930	SBd		×		
N3992	SBbc				
U6940	Scd				
N4013	Sb	×			
U6962	SBcd			×	×
N4010	SBd	×		×	
U6969	Sm				
U6973	Sab	×			×
U6983	SBcd				
N4051	SBbc			×	
N4085	Sc			×	
N4088	Sbc	×	×	×	
U7089	Sdm		×		
N4100	Sbc	×			
U7094	Sdm		×		
N4102	SBab				
N4117	S0				
N4138	Sa	×	×		
N4157	Sb	×			
N4183	Scd	×			
N4218	Sm				
N4217	Sb				
N4220	Sa				
N4389	SBbc				

brightness can be discerned. However, in the lower row, the profiles are grouped according to the galaxy properties as listed in Table 6. In this case, a clear trend is visible in the sense that galaxies with high HI surface densities in their inner regions are either involved in interactions, are lopsided or display a warped HI disk. Especially in the case of interacting and strongly lopsided systems, no longlived stable gas orbits can be expected and evidently,

the cold gas becomes concentrated toward the inner regions of the disk. Note that some galaxies appear in more than one panel.

Warps are thought to be a quite common feature of the outer HI layers of spiral galaxies. But, in spite of attempts made in recent years (Bosma, 1991), a good statistics on their occurrence does not exist yet. The information on HI warps provided by the present survey of the Ursa Major sample is somewhat limited mainly because of the already noted small radial extent of the HI layers with respect to the optical. There are pronounced HI warps like the well-known ones found in NGC 3718 (Schwarz 1985) and NGC 4013 (Bottema 1995) and those seen in other galaxies (N3726, N3985, N4010, N4157, N4183). In most cases the warps are visible in the outer parts beyond the optical bright disk and are present in normal, regular, not interacting disks. But there are also systems, like NGC 4088, which are strongly distorted in their optical appearance and also in their kinematics. Similar distortions are found in clearly interacting systems like NGC 3769. In the sample of 43 galaxies (Table 6) there are at least 13 objects with clear indications of warping.

Also asymmetries are thought to occur frequently in field spirals (Richter and Sancisi, 1994). In the present sample we see a large number of objects (at least half, see Table 6) with a lopsided HI distribution and/or kinematics. The majority shows kinematical asymmetries: on one side of the disk the rotation curve rises more slowly and reaches its flat part at a larger radius than on the other side (see for example NGC 3877, 3949, 4051). Note that this occurs in the inner parts of non-interacting, regular, normal systems.

Finally, there are four galaxies in this sample of 43 which have close companions and show clear HI signs of tidal interactions. A few more objects (examples NGC 3718, 4088) show distortions or peculiar structures in their density and velocity maps.

## 8. Concluding remarks

This data paper has presented the results of an extensive HI synthesis imaging survey with the WSRT of a well-defined complete equidistant sample of spiral galaxies in the nearby Ursa Major cluster. Figures B.1 and B.2 show a compilation of all the available HI maps. Individual galaxies are at their proper position on the sky but they are individually four times enlarged. Some galaxies had to be shifted to avoid overlapping maps. Rotation curves have been derived for most galaxies as well as detailed information on the kinematical state of the galaxy disks as indicated by the presence of global perturbations, warps, interactions and lopsidedness. Since the galaxies were not selected on the basis of their HI size or content, the quality of the kinematical data varies widely from galaxy to galaxy. Nevertheless, these data will be useful for an analysis of the statistical properties of the Tully-Fisher relation

and the rotation curves may be decomposed into contributions from the main dynamical constituents like the stellar and gaseous disks, the bulge and the dark matter halo. These issues will be addressed in forthcoming papers.

Those who would like to use the rotation curves for their own purposes are advised not to take the rotation curves at face value but to check their validity against the actual data and to take notice of the comments provided on the atlas pages. It should be realized that the rotation curves presented here are derived from the kinematics of the HI gas which is assumed to be a tracer of a galaxy's potential. There are some caveats to be aware of like the projection effects of streaming motions and partially filled HI disks of edge-on systems.

Finally, optical long-slit spectroscopy is already available for nearly all galaxies in the sample. These high resolution optical rotation curves will be used to supplement the HI rotation curves in the inner regions, allowing for better decompositions and maximum-disk constraints.

*Acknowledgements.* The Westerbork Synthesis Radio Telescope is operated by the Netherlands Foundation for Research in Astronomy (NFRA/ASTRON), with financial support by the Netherlands Organization for Scientific Research (NWO). This research has made use of the NASA/IPAC Extragalactic Database (NED) which is operated by the Jet Propulsion Laboratory, Caltech, under agreement with the National Aeronautics and Space Association. The results presented in this paper were obtained during MV's thesis research at the Kapteyn Institute of the University of Groningen, The Netherlands. This paper was finalized at the National Radio Astronomy Observatory which is a facility of the National Science Foundation operated under cooperative agreement by Associated Universities, Inc.

## References

- Appleton, P.N. and Davies, R.D., 1982, MNRAS, 201, 1073
- Begeman, K.G., 1987, Thesis, University of Groningen
- Begeman, K.G., 1989, A&A, 223, 47
- Bosma, A., 1991, "Warped and flaring HI disks", in *"Warped disks and inclined rings around galaxies"*, Casertano, S., Sackett, P. and Briggs, F. (eds), Cambridge University Press, p.181
- Bottema, R., 1995, A&A, 295, 605
- Bottema, R., 1996, A&A, 306, 345
- Bottinelli, L., Gouguenheim, L., Paturel, G. and De Vaucouleurs, G., 1983, A&A, 118, 4
- Bottinelli, L., Gouguenheim, L., Fouqué, P. and Paturel, G., 1990, A&AS, 82, 391
- Bravo-Alfaro, H., Cayatte, V., Van Gorkom, J.H. and Balkowski, C., 2000, AJ, 119, 580
- Broeils, A.H., 1992, Thesis, University of Groningen
- Broeils, A.H. and van Woerden, H., 1994, A&AS, 107, 129
- Burstein, D. and Heiles, C., 1984, ApJS, 54, 33
- Cardelli, J.A., Clayton, G.C. and Mathis, J.S., 1989, ApJ, 345, 245
- Cayatte, V., van Gorkom, J.H., Balkowski, C. and Kotanyi, C.G., 1990, AJ, 100, 604

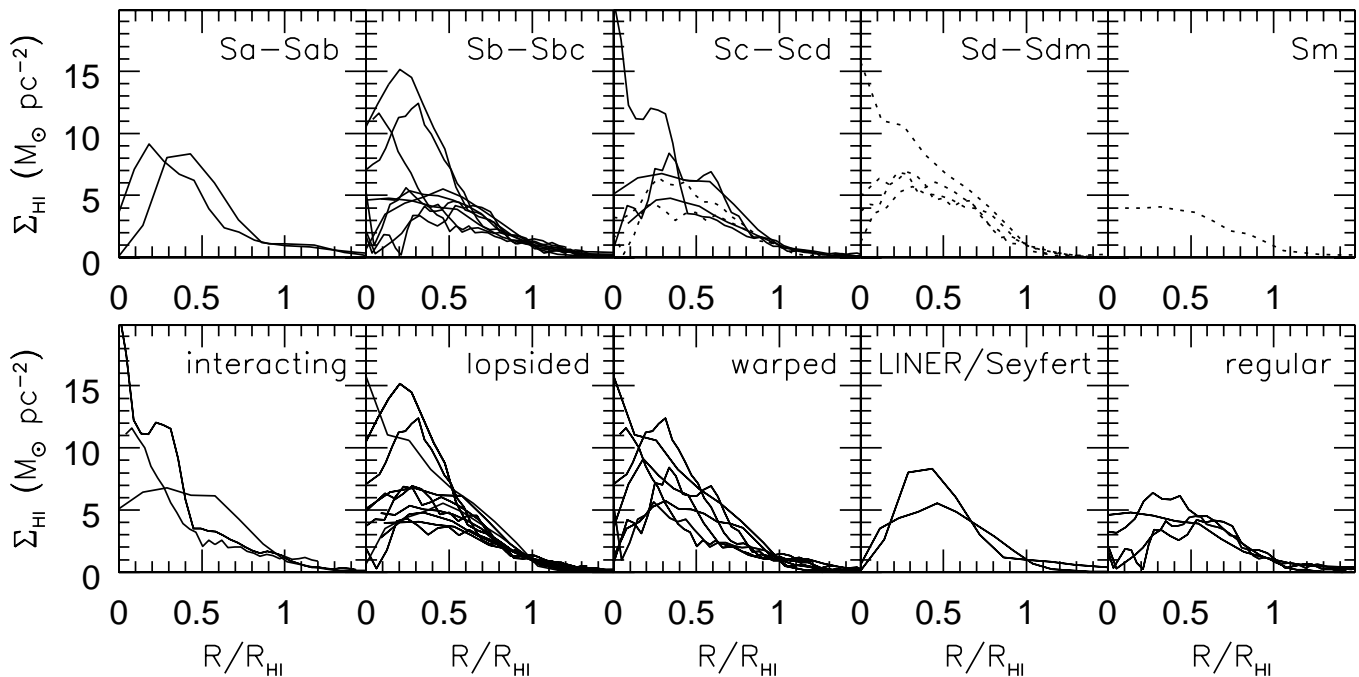


**Fig. 8.** Azimuthally averaged deprojected radial HI surface density profiles of galaxies with fully reduced data, less inclined than 80 degrees and with  $R_{\text{HI}} > 1$  arcmin. The profiles were scaled in radius by the radius of the HI disk measured at the  $1 \text{ M}_{\odot} \text{pc}^{-2}$  isodensity contour. Upper row:  $\Sigma_{\text{HI}}$  as a function of morphological type. The dashed lines indicate low surface brightness galaxies. Lower row:  $\Sigma_{\text{HI}}$  as a function of the kinematic state, according to Table 6, and nuclear activity.

- Cayatte, V., Kotanyi, C.G., Balkowski, C. and van Gorkom, J.H., 1994, *AJ*, 107, 1003
- Dickey, J.M. and Gavazzi, G., 1991, *ApJ*, 373, 347
- Dickey, J.M., 1997, *AJ*, 113, 1939
- Fisher, J.R. and Tully, R.B., 1981, *ApJS*, 47, 139
- Fouqué, P., Bottinelli, L., Gouguenheim, L. and Paturel, G., 1990, *ApJ*, 349, 1
- Gottesman, S.T., Ball, R. and Hunter Jr, J.H., 1984, *ApJ*, 286, 471
- Grewing, M. and Mebold, U., 1975, *A&A*, 42, 119
- Högbom, J.A., 1974, *A&AS*, 15, 417
- Holmberg, E., 1946, *Medd. Lunds Astr. Obs., Ser.II*, No.117
- Hubble, E., 1926, *ApJ*, 64, 321
- Huchtmeier, W.K. and Richter, O.-G., 1986, *A&AS*, 63, 323
- Jore, K.P., Broeils, A.H. and Haynes, M.P., 1996, *AJ*, 112, 438
- Lucy, L.B., 1974, *AJ*, 79, 745
- Magri, C., 1994, *AJ*, 108, 896
- McMahon, P.M., 1993, Thesis, University of Columbia
- Navarro, J.F. and Steinmetz M., 2000, *ApJ*, 538, 477
- Oosterloo, T. and Shostak, S., 1993, *A&AS*, 99, 379
- Puche, D. and Garignan, C., 1991, *AJ*, 378, 487
- Rhee, M.-H., 1996a, Thesis, University of Groningen
- Rhee, M.-H., 1996b, *A&AS*, 115, 407
- Richter, O.-G. and Huchtmeier, W.K., 1991, *A&AS*, 87, 425
- Richter, O.-G. and Sancisi, R., 1994, *A&A*, 295, 605
- Roberts, M.S. and Haynes, M.P., 1994, *ARA&A*, 32, 115
- Sakai, S., Mould, J.R., Hughes, S.M.G., Macri, L.M., Kennicutt, R.C. Jr., et al., 2000, *ApJ*, 529, 698
- Sancisi, R. and Allen, R.J., 1979, *A&A*, 74, 73
- Schlegel, D.J., Finkbeiner, D.P. and Davis, M., 1998, *ApJ*, 500, 525
- Schneider, S.E., Thuan, T.X., Mangum, J.G. and Miller, J., 1992, *ApJS*, 81, 5
- Schwarz, U.J., 1985, *A&A*, 142, 273
- Swater, R.A., 1999, "Dark Matter in late type dwarf galaxies", Ph.D. Thesis, University of Groningen
- Thuan, T.X. and Martin, G.E., 1981, *ApJ*, 247, 823
- Tully, R.B. and Fouqué, P., 1985, *ApJS*, 58, 67 (TFq)
- Tully, R.B., Verheijen, M.A.W., Pierce, M.J., Huang, J.-S. and Wainscoat, R.J., 1996, *AJ*, 112, 2471 (Paper I)
- Tully, R.B. and Verheijen, M.A.W., 1997, *ApJ*, 484, 145 (Paper II)
- Tully, R.B., Pierce, M.J., Huang, J.-S., Saunders, W., Verheijen, M.A.W. and Witchalls, P.L., 1998, *AJ*, 115, 2264
- Tully, R.B. and Pierce, M.J., 2000, *ApJ*, 533, 744
- Van der Burg, G., 1987, Ph.D. Thesis, University of Groningen
- Van Moorsel, G.A., 1983, *A&AS*, 54, 1
- Warmels, R.H., 1988a, *A&AS*, 72, 19
- Warmels, R.H., 1988b, *A&AS*, 72, 57

**Appendix A: The noise in an integrated HI map.**

This appendix explains how the noise in a total HI map can be calculated. A total HI map is usually constructed from a 3 dimensional datacube containing a number of so called channelmaps. Each channelmap shows an HI image of the galaxy at a certain velocity. A total HI map is made by adding those channelmaps which contain the HI signal. Before adding the channel maps the signal in each channelmap should be isolated. When the signal is not isolated one merely adds noise to the total HI map because the location of the signal in a channel map varies with velocity due to the galactic rotation. The signals can be isolated interactively by blotting away the surrounding noise or in a more objective way by taking a certain contour level in the smoothed maps as a mask. As a consequence of adding channel maps with isolated regions, the noise in the total HI map is not constant but varies from pixel to pixel. The noise at a certain pixel in the total HI map depends on the number N of non-blank pixels at the same position in the individual channel maps that were added.

In case the data cube was obtained with an uniform taper during the observation, the noise  $\sigma^u$  in two channelmaps will be independent. The noise equivalent bandwidth  $B^u$  in a uniform tapered spectrum is equal to the channel separation  $b$ . When adding N uniform tapered channelmaps at a certain pixel the noise  $\sigma_N^u$  at the same pixel position in the total HI map will be increased by a factor  $\sqrt{N}$ :

$$\sigma_N^u = \sqrt{N} \sigma^u$$

Usually, the observations are made using a hanning taper in which case the noise in two adjacent channelmaps is no longer independent. A hanning taper effectively smooths the data in velocity by convolving the velocity profile at each pixel. If  $U_i$  is the pixel value in the  $i^{th}$  uniform tapered channel map, the value  $H_i$  in the  $i^{th}$  hanning tapered channelmap is given by

$$H_i = \frac{1}{4}U_{i-1} + \frac{1}{2}U_i + \frac{1}{4}U_{i+1}$$

Since the  $\sigma_i^u$ 's are independent and all equal to  $\sigma^u$ , the noise  $\sigma_i^h$  in the  $i^{th}$  hanning tapered channelmap can be calculated according to

$$\begin{aligned} \sigma_i^h &= [(\frac{1}{4}\sigma_{i-1}^u)^2 + (\frac{1}{2}\sigma_i^u)^2 + (\frac{1}{4}\sigma_{i+1}^u)^2]^{\frac{1}{2}} \\ &= [\frac{1}{16} + \frac{1}{4} + \frac{1}{16}]^{\frac{1}{2}} \sigma^u \\ &= \frac{\sqrt{6}}{4} \sigma^u = 0.61 \sigma^u \end{aligned}$$

In this case the noise equivalent bandwidth  $B^h$  for a hanning tapered spectrum is given by

$$B^h = \frac{16}{6} B^u = 2.67 B^u$$

As a consequence, the noise in two hanning tapered channelmaps may be correlated depending on their separation. Two channelmaps separated by one channelmap are correlated because both contain a quarter of the flux from the channel map between them. Only channel maps separated by more than one channel are independent. This will be shown in the following three cases in which two hanning tapered channel maps at different separations will be added.

1. Adding two adjacent hanning tapered channelmaps  $i$  and  $(i+1)$  gives a signal  $H_{(i)+(i+1)}$  of

$$\begin{aligned} H_{(i)+(i+1)} &= H_i + H_{i+1} \\ &= (\frac{1}{4}U_{i-1} + \frac{1}{2}U_i + \frac{1}{4}U_{i+1}) \\ &\quad + (\frac{1}{4}U_i + \frac{1}{2}U_{i+1} + \frac{1}{4}U_{i+2}) \\ &= \frac{1}{4}U_{i-1} + \frac{3}{4}U_i + \frac{3}{4}U_{i+1} + \frac{1}{4}U_{i+2} \end{aligned}$$

and the noise  $\sigma_{(i)+(i+1)}^h$  in that map will be

$$\begin{aligned} \sigma_{(i)+(i+1)}^h &= [(\frac{1}{4}\sigma_{i-1}^u)^2 + (\frac{3}{4}\sigma_i^u)^2 \\ &\quad + (\frac{3}{4}\sigma_{i+1}^u)^2 + (\frac{1}{4}\sigma_{i+2}^u)^2]^{\frac{1}{2}} \\ &= \frac{\sqrt{20}}{4} \sigma^u = \frac{\sqrt{20}}{4} \frac{4}{\sqrt{6}} \sigma^h \\ &= \sqrt{3\frac{1}{3}} \sigma^h = 1.83 \sigma^h \end{aligned}$$

2. Adding the hanning tapered channels  $i$  and  $(i+2)$  gives

$$\begin{aligned} H_{(i)+(i+2)} &= H_i + H_{i+2} \\ &= (\frac{1}{4}U_{i-1} + \frac{1}{2}U_i + \frac{1}{4}U_{i+1}) \\ &\quad + (\frac{1}{4}U_{i+1} + \frac{1}{2}U_{i+2} + \frac{1}{4}U_{i+3}) \\ &= \frac{1}{4}U_{i-1} + \frac{1}{2}U_i + \frac{1}{2}U_{i+1} \\ &\quad + \frac{1}{2}U_{i+2} + \frac{1}{4}U_{i+3} \end{aligned}$$

and the noise becomes

$$\begin{aligned} \sigma_{(i)+(i+2)}^h &= [(\frac{1}{4}\sigma_{i-1}^u)^2 + (\frac{1}{2}\sigma_i^u)^2 + (\frac{1}{2}\sigma_{i+1}^u)^2 \\ &\quad + (\frac{1}{2}\sigma_{i+2}^u)^2 + (\frac{1}{4}\sigma_{i+3}^u)^2]^{\frac{1}{2}} \\ &= \frac{\sqrt{14}}{4} \sigma^u = \frac{\sqrt{14}}{4} \frac{4}{\sqrt{6}} \sigma^h \\ &= \sqrt{2\frac{1}{3}} \sigma^h = 1.53 \sigma^h \end{aligned}$$

3. Adding the hanning tapered channels  $i$  and  $(i+3)$  gives

$$\begin{aligned} H_{(i)+(i+3)} &= H_i + H_{i+3} \\ &= (\frac{1}{4}U_{i-1} + \frac{1}{2}U_i + \frac{1}{4}U_{i+1}) \\ &\quad + (\frac{1}{4}U_{i+2} + \frac{1}{2}U_{i+3} + \frac{1}{4}U_{i+4}) \end{aligned}$$

with a resulting noise of

$$\begin{aligned}\sigma_{(i)+(i+3)}^h &= \left[ \left(\frac{1}{4}\sigma_{i-1}^u\right)^2 + \left(\frac{1}{2}\sigma_i^u\right)^2 + \left(\frac{1}{4}\sigma_{i+1}^u\right)^2 \right. \\ &\quad \left. + \left(\frac{1}{4}\sigma_{i+2}^u\right)^2 + \left(\frac{1}{2}\sigma_{i+3}^u\right)^2 + \left(\frac{1}{4}\sigma_{i+4}^u\right)^2 \right]^{\frac{1}{2}} \\ &= \frac{\sqrt{12}}{4} \sigma^u = \frac{\sqrt{12}}{4} \frac{4}{\sqrt{6}} \sigma^h \\ &= \sqrt{2} \sigma^h = 1.41 \sigma^h\end{aligned}$$

So, channelmaps  $i$  and  $(i+3)$  are independent.

Because the noise is correlated, adding  $N$  *adjacent* hanning tapered channelmaps does not give an increase of the noise with a factor  $\sqrt{N}$  but with a factor  $\sqrt{N - \frac{3}{4}} \cdot \frac{4}{\sqrt{6}}$  as is shown below. First the total signal  $H_N$  is calculated.

Channel	$U_{i-1}$	$U_i$	$U_{i+1}$	$\dots$	$U_{i+N-2}$	$U_{i+N-1}$	$U_{i+N}$
$i$	$1/4$	$1/2$	$1/4$	$\dots$			
$i+1$		$1/4$	$1/2$	$\dots$			
$i+2$			$1/4$	$\dots$			
$\dots$				$\dots$			
$i+N-3$				$\dots$	$1/4$		
$i+N-2$				$\dots$	$1/2$	$1/4$	
$i+N-1$				$\dots$	$1/4$	$1/2$	$1/4$
	$\frac{1}{4}U_{i-1}$	$\frac{3}{4}U_i$	$U_{i+1}$	$\dots$	$U_{i+N-2}$	$\frac{3}{4}U_{i+N-1}$	$\frac{1}{4}U_{i+N}$

and thus

$$H_N = \frac{1}{4}U_{i-1} + \frac{3}{4}U_i + U_{i+1} + \dots + U_{i+N-2} + \frac{3}{4}U_{i+N-1} + \frac{1}{4}U_{i+N}$$

From this it follows that the noise  $\sigma_N^h$  is given by

$$\begin{aligned}\sigma_N^h &= \left[ \left(\frac{1}{4}\right)^2 + \left(\frac{3}{4}\right)^2 + (N-2) \cdot 1^2 + \left(\frac{3}{4}\right)^2 + \left(\frac{1}{4}\right)^2 \right]^{\frac{1}{2}} \sigma^u \\ &= \left[ N - \frac{3}{4} \right]^{\frac{1}{2}} \sigma^u = \left[ N - \frac{3}{4} \right]^{\frac{1}{2}} \frac{4}{\sqrt{6}} \sigma^h \\ &= \sqrt{\left(N - \frac{3}{4}\right) B^h} \sigma^h\end{aligned}$$

However, before the hanning tapered channelmaps are added to form a total HI map, the continuum must be subtracted. This operation introduces extra noise in the channelmaps which doesn't behave like a hanning tapered correlation. Here, it will be assumed that the average continuum map is formed by averaging  $N_1$  line free channels at the low velocity end of the datacube and  $N_2$  channels at the high velocity end which gives

$$C_{low} = \frac{1}{N_1} \sum_{j=1}^{N_1} H_j \quad \text{and} \quad C_{high} = \frac{1}{N_2} \sum_{j=1}^{N_2} H_j$$

Since all channels are hanning tapered the noise in these maps can be calculated according to

$$\sigma_{C_{low}} = \frac{1}{N_1} \sqrt{\left(N_1 - \frac{3}{4}\right)} \sigma^u$$

and

$$\sigma_{C_{high}} = \frac{1}{N_2} \sqrt{\left(N_2 - \frac{3}{4}\right)} \sigma^u$$

The average continuum map to be subtracted is then formed by

$$\langle C \rangle = \frac{1}{2}(C_{low} + C_{high})$$

Since  $\sigma_{C_{low}}$  and  $\sigma_{C_{high}}$  are independent it follows that the noise  $\sigma_{\langle C \rangle}$  in the finally averaged continuum map is given by

$$\begin{aligned}\sigma_{\langle C \rangle} &= \frac{1}{2} \sqrt{\sigma_{C_{low}}^2 + \sigma_{C_{high}}^2} \\ &= \sigma^u \sqrt{\left(\frac{N_1 - \frac{3}{4}}{4N_1^2} + \frac{N_2 - \frac{3}{4}}{4N_2^2}\right)} \\ &\equiv \sigma^u \mathcal{N}\end{aligned}$$

After subtraction of the continuum the channelmaps only contain signal from the HI emission line. The signal in the channelmaps containing the line emission is now given by

$$\begin{aligned}L_i &= H_i - \langle C \rangle \\ &= \frac{1}{4}U_{i-1} + \frac{1}{2}U_i + \frac{1}{4}U_{i+1} - \langle C \rangle\end{aligned}$$

Because  $\sigma_{\langle C \rangle}$  is independent from  $\sigma_i^u$  in the velocity range which is not used to form the averaged continuum map, it can be written

$$\begin{aligned}\sigma_i^l &= \left[ \left(\frac{1}{4}\sigma_{i-1}^u\right)^2 + \left(\frac{1}{2}\sigma_i^u\right)^2 + \left(\frac{1}{4}\sigma_{i+1}^u\right)^2 + \sigma_{\langle C \rangle}^2 \right]^{\frac{1}{2}} \\ &= \left[ \frac{1}{16} + \frac{4}{16} + \frac{1}{16} + \mathcal{N}^2 \right]^{\frac{1}{2}} \sigma^u \\ &= \sqrt{\left(\frac{3}{8} + \mathcal{N}^2\right)} \sigma^u\end{aligned}$$

When adding  $N$  *adjacent* hanning tapered and continuum subtracted channelmaps containing the line emission, the signal  $L_N$  will be

$$\begin{aligned}L_N &= \frac{1}{4}U_{i-1} + \frac{3}{4}U_i + U_{i+1} + \dots \\ &\quad \dots + U_{i+N-2} + \frac{3}{4}U_{i+N-1} + \frac{1}{4}U_{i+N} \\ &\quad - N \cdot \langle C \rangle\end{aligned}$$

The noise  $\sigma_N^l$  at each pixel in the final map can be derived analogous to the calculation of  $\sigma_N^h$  and is given by

$$\begin{aligned}\sigma_N^l &= \left[ \left(N - \frac{3}{4}\right) + N^2 \mathcal{N}^2 \right]^{\frac{1}{2}} \sigma^u \\ &= B^h \sqrt{\left(\frac{\left(N - \frac{3}{4}\right) + N^2 \mathcal{N}^2}{B^h}\right)} \sigma^h\end{aligned}$$

Appendix B: The HI Atlas

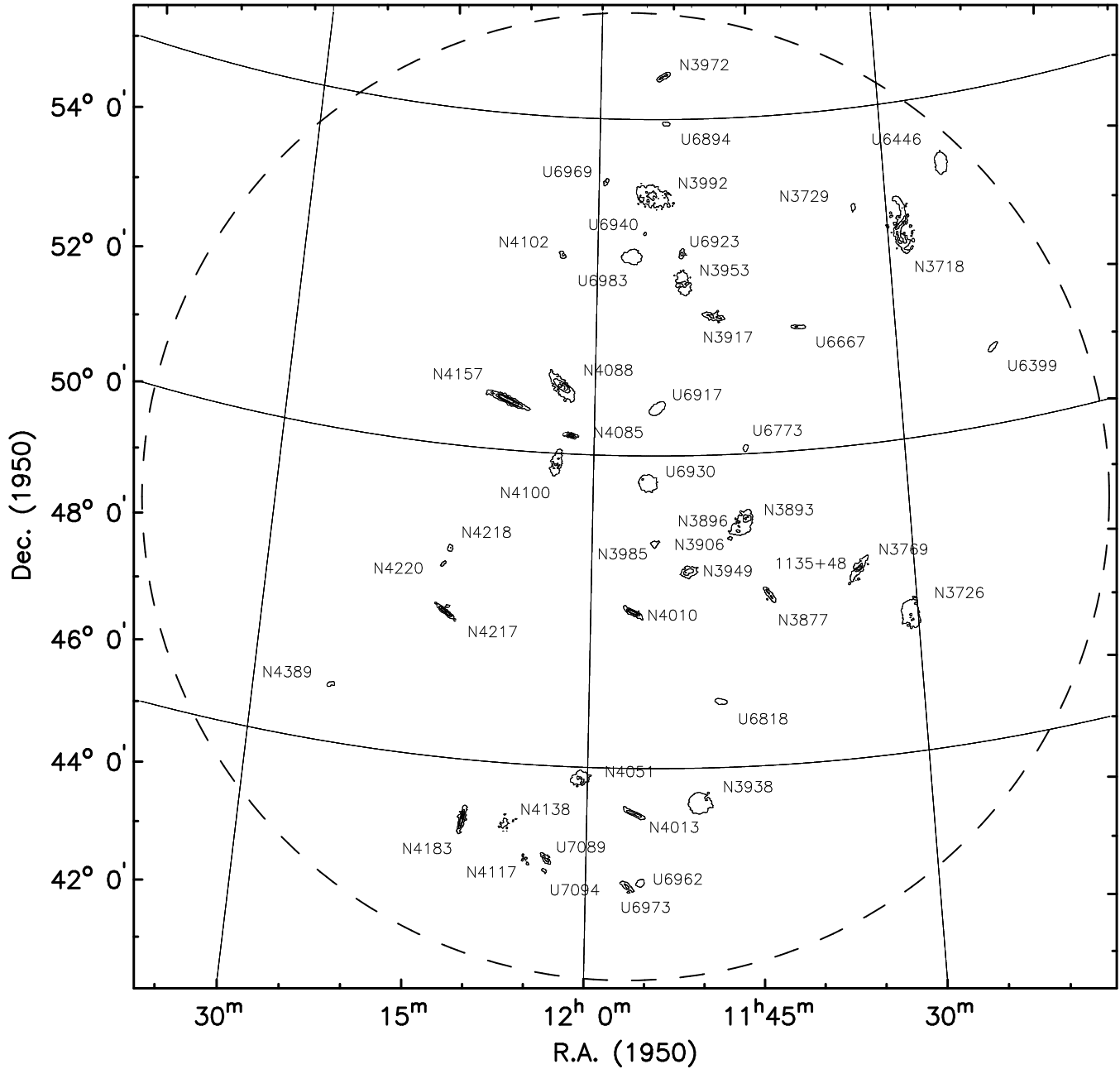


**Fig. B.1.** Integrated HI maps of all galaxies in the cluster more inclined than 45 degrees and brighter than  $M(B)=-16.5$ . The angular resolution is  $30 \times 30$  arcsec. Contour levels are at column densities of 0.5, 2.0, 3.5 and  $5.0 \times 10^{21}$  atoms  $\text{cm}^{-2}$ . Individual galaxies are four times enlarged. To avoid overlap, some galaxies are slightly displaced from their actual position. N3906, N3938, U6962 and U6930 are more face-on than 45 degrees. U6940 is fainter than the complete sample limit. The dashed circle indicates the adopted boundary of the cluster.

**Fig. B.2.** Same as figure 1, displayed here in grayscale. Note the interacting pairs N3769/1135+48, N3893/N3896 and U6962/U6973. The galaxies N3718, N3726, N4010, N4013, N4088 and N4138 are strongly warped. It is clear that the integrated column density strongly depends on inclination. Many of the more face-on galaxies show a depletion of the HI gas in their inner regions.

Observing parameters for UGC 6399

Length of observation (hours)	1 × 12
Dates of observation	6Aug90
Field center, $\alpha$ (1950)	11:20:30
$\delta$ (1950)	51:10:00
Central frequency (MHz)	1416.56
$V_{\text{hel}}$ of central channel ( $\text{km s}^{-1}$ )	810
Primary beam FWHM (arcmin)	37.4
Nr. of interferometers	40
Baselines (min-max-incr) (m)	36-2700-72
Synthesized beam ( $\alpha \times \delta$ )(arcsec)	12.9 × 16.6
Bandwidth (MHz)	2.5
Number of channels	127
Channel separation ( $\text{km s}^{-1}$ )	4.15
Velocity resolution ( $\text{km s}^{-1}$ )	8.29
rms noise in one channel (K)	5.54
K-mJy conversion, equiv. of 1mJy/beam (K)	2.84

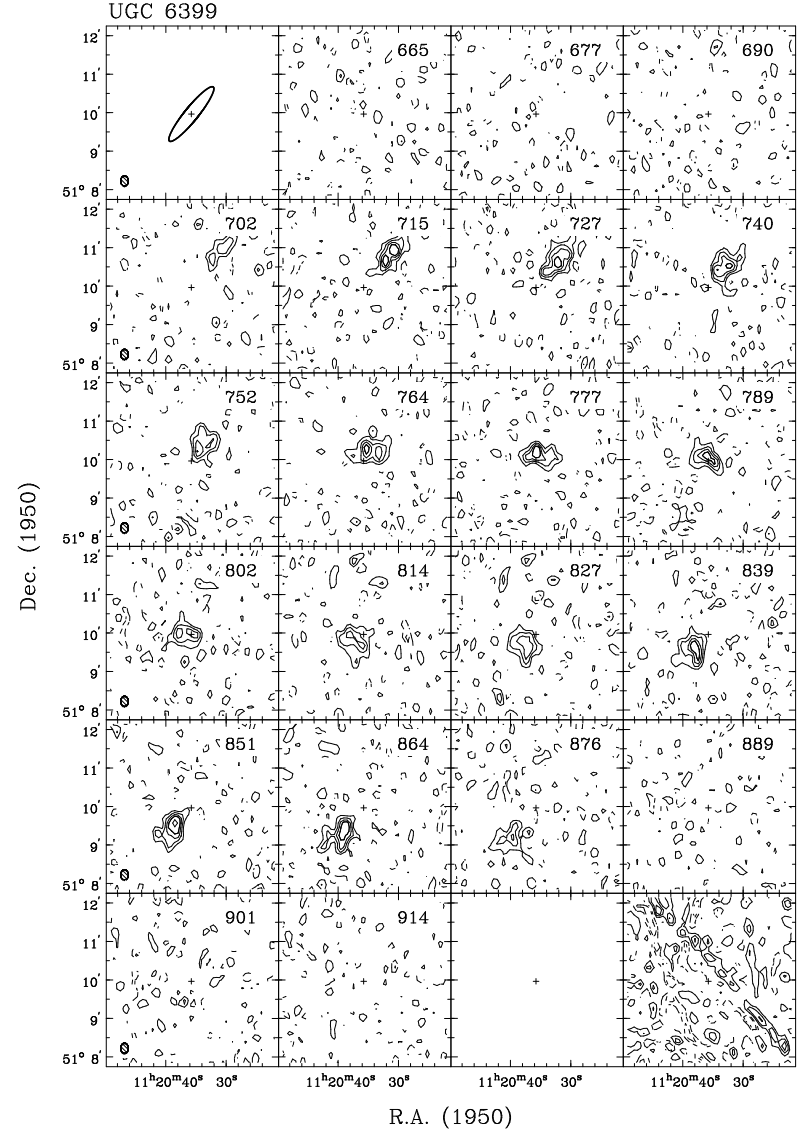
Contour levels for U6399

Channel maps:	$\sigma=3.55$ (K)
Raw continuum map:	$\sigma=1.35$ (K)
Cleaned continuum map:	$\sigma=1.19$ (K)
Position-Velocity diagrams:	$\sigma=3.12$ (K)
Velocity fields:	$794.5 \pm n \times 15$ ( $\text{km s}^{-1}$ )
Residual velocity field:	$\pm n \times 5$ ( $\text{km s}^{-1}$ )
Integrated HI map:	0.52, 1.04, $1.56 (\times 10^{21} \text{ atoms cm}^{-2})$

Results from WSRT data

<u>From continuum map:</u>	
21-cm flux density:	
central point source (mJy)	<1.3 ( $3\sigma$ )
extended source (mJy)	<2.5 ( $3\sigma$ )
<u>From global profile:</u>	
Integrated HI-flux ( $\text{Jy km s}^{-1}$ )	$10.5 \pm 0.3$
Hel. systemic velocity ( $\text{km s}^{-1}$ )	$791.5 \pm 0.6$
HI profile width, 20% ( $\text{km s}^{-1}$ )	$188.1 \pm 1.4$
50% ( $\text{km s}^{-1}$ )	$172.5 \pm 2.9$
<u>From velocity field:</u>	
Hel. systemic velocity ( $\text{km s}^{-1}$ )	$794.5 \pm 1.3$
Dynamical center, $\alpha$ (1950)	11:20:35.8
$\delta$ (1950)	51:09:58
<u>From total HI map:</u>	
Geometric center, $\alpha$ (1950)	11:20:35.7
$\delta$ (1950)	51:10:01
Position angle (deg)	139
Inclination angle (deg)	77
Diameter of HI disk (arcmin)	3.4

**Note:** This is the most isolated system in the cluster. The rotation curve does not show a flat part on the receding side and maybe just barely on the approaching side.



Channel maps at a resolution of  $12'' \times 16'' \times 19 \text{ km s}^{-1}$ . Contour levels at -3, -1.5 (dashed), 1.5, 3, 4.5, ...  $\times \sigma$ .



